Integrating outcomes from probabilistic and deterministic seismic hazard analysis in the Tien Shan

I. Mosca[1], B. Baptie [1], S. Sargeant [1], R. T. Walker [2]

[1] British Geological Survey, the Lyell Centre, Research Avenue South, Edinburgh EH14 4AP, United Kingdom

[2] COMET, Department of Earth Sciences, Oxford University, South Parks Road, Oxford OX1 3AN, United Kingdom

Abstract

In this study, we have evaluated the probabilistic and deterministic seismic hazard for the city of Almaty, the largest city in Kazakhstan, which has a population of nearly 2 million people. Almaty is located in the Tien Shan mountain belt, a low strain rate environment within the interior of the Eurasian plate that is characterized by large, infrequent earthquakes. A robust assessment of seismic hazard for Almaty is challenging because current knowledge about the occurrence of large earthquakes is limited due to the short duration of the earthquake catalogue and only partial information about the geometry, rupture behaviour, slip rate, and the maximum expected earthquake magnitude of the faults in the area. The impact that this incomplete knowledge has on assessing seismic hazard in this area can be overcome by using both probabilistic and deterministic approaches and integrating the results.

First, we simulate ground shaking scenarios for three destructive historical earthquakes that occurred in the Northern Tien Shan in 1887, 1889 and 1911, using ground motion prediction equations (GMPEs) and realistic fault rupture models based on recent geomorphological studies. We show that the large variability in the GMPEs results in large uncertainty in the ground motion simulations. Then, we estimate the seismic hazard probabilistically using a Monte Carlo-based PSHA and the earthquake catalogue compiled from the databases of the International Seismological Centre and the British Geological Survey. The results show that earthquakes of Mw 7.0 to 7.5 at Joyner-Boore distances of less than 10 km from the city pose a significant hazard to Almaty due to their proximity. These potential future earthquakes are similar to the 1887 Verny earthquake in terms of their magnitude and distance from Almaty. Unfortunately, this is the least well understood of the destructive historical earthquakes that have occurred in the Northern Tien Shan.

Introduction

The Tien Shan is situated in a low strain region in the interior of the Eurasian plate (e.g., Landgraf et al., 2016a). Slip on faults accumulates at rates of less than a few millimeters per year compared with plate boundaries where slip rates reach 10-100 mm/yr (England and Jackson, 2011). In the Tien Shan, there are many segmented faults that form a zone hundreds of kilometers wide. The time required to accumulate the tectonic displacement is from a few hundreds to a few thousands of years due to the low strain rate and the low tectonic loading (e.g., England and Jackson, 2011; Landgraf et al., 2016b). For this reason, earthquakes of moment magnitude (Mw) > 7 are infrequent here and their recurrence intervals are up to thousands of years (e.g., Abdrakhmatov et al., 2016; Landgraf et al., 2016a). Furthermore, most of these faults are poorly understood or unknown until an earthquake occurs along them (e.g., England and Jackson, 2011; Liu and Stein, 2016). Recent studies, based on geomorphological and paleoseismological data, have become available for some areas of the Tien Shan. They can be used to extend the earthquake records back in time (e.g., Landgraf et al., 2016a; Grützner et al., 2017) by mapping and characterizing probable surface ruptures associated with the historical earthquakes that occurred between 1885 and 1911 in the Northern Tien Shan (Arrowsmith et al., 2016; Abdrakhmatov et al., 2016).

Seismic hazard assessment for this region is challenging because the available seismological data do not adequately represent the long-term earthquake history in the region (e.g., Abdrakhmatov et al., 2016; Landgraf et al., 2016a). As a result, the undertaking of either probabilistic seismic hazard analysis (PSHA; e.g., Reiter, 1990; McGuire, 2004) or deterministic seismic hazard analysis independently (DSHA; e.g., Reiter, 1990) may be insufficient for this region. Instead, integrating the outcomes from PSHA and DSHA may produce a more rigorous seismic hazard assessment. The goal of this paper is to combine the outcomes from both PSHA and DSHA to address the lack of 'sufficient' seismological and geological data for this area. First, we evaluate the deterministic scenarios and then compute the hazard using a probabilistic approach in order to estimate the annual frequency of exceedance of the deterministic ground motion value(s). Then, we check the results of the probabilistic analysis with DSHA to determine the credible earthquake scenario for low annual frequencies of exceedance. Using both PSHA and DSHA is recommended for the seismic hazard of highly critical infrastructure, such as nuclear power plants (IAEA, 2010), where the standard practice is to perform PSHA and then to apply DSHA for the scenario of the maximum credible earthquake that is the reasonably largest earthquake. There are also studies that combine the PSHA and the DSHA for region-based seismic hazard analysis (e.g., Wong et al., 2002).

This study focuses on Almaty, the former capital of Kazakhstan and the largest city in the region (Figure 1). It is situated in a topographical depression in the foothills of the Zailisky Alatau mountain ranges that are bounded by poorly understood and sometimes unmapped faults (Pilz et al., 2015; Grützner et al., 2017). The building profile of the city is ever-changing and many new buildings have been constructed in the last 30 years including residential buildings of four to nine stories (King et al., 1999) and buildings of up to 38-stories, such as Almaty Towers and Esentai Tower (Paramzin, 2005). The population of Almaty has increased from a few thousands of people at the beginning of the 20th century to almost two million in 2017 (Silacheva et al., 2017). This rapid growth has increased both the number of people and assets exposed to the earthquake risk. This requires using techniques that allow for a robust estimate of the seismic hazard due to our incomplete understanding of the earthquake environment in this region.

The mapping and characterization of the surface ruptures for the historical earthquakes that occurred between 1887 and 1911 in the Northern Tien Shan from the recent studies of Arrowsmith et al. (2016) and Abdrakhmatov et al. (2016) allows now for such a seismic hazard re-estimation to take place. These mapped faults are the basis for realistic fault rupture models using DSHA. Then, we perform a PSHA to determine the return periods for different levels of the scenario ground shaking for a site in Almaty. The hazard results obtained from the PSHA are disaggregated to show the contribution of future earthquakes similar to the historical earthquakes to the overall hazard of Almaty.

Regional setting

The Tien Shan is a tectonically and seismically active intraplate mountain belt that is bounded by the Kyzyl-Kum desert to the east and the Gobi Desert to the west, and lies between the Kazakh Platform to the north and the Tarim Basin to the south (Figure 1).

The formation of this mountain belt is a consequence of the continental collision between the Indian and Eurasian plates that started ~50 Ma ago. This resulted in the reactivation of pre-Cenozoic structures in the last 50 Ma in Central Asia, including the Tien Shan, (e.g., Tapponnier and Molnar, 1979; Burtman et al., 1996). The present-day crustal shortening across the Tien Shan is ~20 mm/yr, corresponding to 40% of the crustal shortening between India and Eurasia, even though the mountain belt is situated more than 1000 km north of the plate boundary (e.g., De Mets et al., 1990; Zubovich et al., 2010). This deformation is accommodated by E-W oriented thrusts, NNW-SSE-trending right-lateral strike-slip faults, and ENE-WSW-trending left-lateral strike-slip faults (e.g., Tapponnier and Molnar, 1979; Thompson et al., 2002; Abdrakhmatov et al., 2016). The E-W-striking faults delineate the E-W-trending mountain ranges and the sub-parallel intra-mountain basins (e.g., Tapponnier and

Molnar, 1979; Thompson et al., 2002). The major strike-slip structure in the Northern Tien Shan is the NNW-SSE-oriented right-lateral strike-slip Talas-Ferghana fault. It accommodates part of the N-S shortening in the Tien Shan with different rates of convergence between the western and eastern Tien Shan (Alinaghi and Krüger, 2014; Campbell et al., 2013).

SEISMICITY IN THE NORTHEN TIEN SHAN

The seismicity in the Tien Shan mountain belt is characterized by a large number of earthquakes of Mw < 7 and 13 seismic events of Mw ≥ 7 since 1875. Since fault slip is accumulated slowly in a low strain rate environment, the recurrence intervals of large earthquakes on active faults in the Tien Shan are likely to exceed the length of the historical earthquake record and so the seismicity catalogue presents an incomplete picture of the earthquake environment (e.g., Abdrakhmatov et al., 2016; Landgraf et al., 2016a). In similar tectonic settings, the identification of hazardous faults that often remain unmapped (2010 Canterbury earthquake in New Zealand; Landgraf et al., 2016b) or for which threat had not been recognized (2003 Bam earthquake; England and Jackson, 2011) further complicates any attempt to assess the seismic hazard. This is because the diffuse network of widespread, highly-segmented faults in low rate environments, is much less well defined than the narrow fault zones found along the plate boundaries (England and Jackson, 2011; Liu and Stein, 2016).

The seismicity in the Tien Shan is associated with faults bounding the intra-mountain basins (e.g., Lake Issyk-Kul and the Ferghana Basin) and tend not to occur within the basins (Zubovich et al., 2010; Alinaghi and Krüger, 2014) (Figure 1). The largest historical earthquakes in the region occurred along the northern (i.e., 1885 surface wave magnitude [Ms] 6.9 Belovodsk; 1887 Ms 7.3 Verny; 1889 Ms 8.3 Chilik; 1911 Ms 8.0 Chon-Kemin) and southern margins of the Tien Shan (e.g., 1902 Ms 8.3 Artux). High levels of instrumental seismicity with magnitudes smaller than Mw 7.0 are located along the margin between the Tien Shan and the Tarim Basin and to a lesser extent, along the margin between the Tien Shan and the Kazakh Platform (Alinaghi and Krüger, 2014) (Figure 1). The largest instrumental earthquakes are the 19 August 1992 Ms 7.3 Suusamyr earthquake and the 24 March 1978 Mw 6.9 Dzhalanash-Tyup earthquake (Figure 1). The 1992 Suusamyr earthquake sequence is the first well-recorded seismic sequence in the region (Ghose et al., 1997; Mellors et al., 1997).

Levels of seismicity of Mw < 6 are associated with the Talas-Ferghana fault and no major earthquakes have occurred along this fault in the last 200 years (Campbell et al., 2013). Ghose et al. (1998) suggest that the lack of large earthquakes on the Talas-Ferghana fault is due to its locked state and present-day activity is accommodated along neighboring compressional structures. The 2 November 1946 Mw 7.6 Chatkal earthquake might have occurred along the Talas-Ferghana fault (e.g., Molnar and Deng, 1984). However, the large uncertainties in the epicentral location and the style of faulting of this earthquake make this hypothesis debatable.

The general tectonic regime in the Tien Shan is compressional and the dominant focal mechanisms are reverse faulting with various degrees of strike-slip motion (Alinaghi and Krüger, 2014). The P-axis of focal mechanisms for the earthquakes in the region is oriented N-S, in agreement with the direction of the convergence between India and Eurasia (e.g., Tapponnier and Molnar, 1979; Alinaghi and Krüger, 2014). There are also a few strike-slip events (e.g., the 12 November 1990 Mw 6.3 earthquake and the 28 January 2013 Mw 6.2 earthquake) that occurred along the margin between the Tien Shan and the Tarim Basin and between the Northern Tien Shan and the Ili Basin.

Sloan et al. (2011) use inversion of teleseismic body waves, identification of depth phases and modeling of regional waveforms, to relocate 123 earthquakes with Mw ≥ 5.2 in the Tien Shan region. They find that hypocentral depths for earthquakes in the Tien Shan mountain belt are in the upper crust at depths of less than 25 km, whereas the earthquakes in the Tien Shan Foreland, the Kazakh Platform, and the Tarim Basin are of the mid to lower crustal nature (up to 40 km hypocentral depth). This may suggest the presence of remnants of subducting plate or underplating involved in the formation of the Tien Shan (Alinaghi and Krüger, 2014).

Deterministic approach

DSHA is generally based on discrete, single-valued models to arrive at scenario-like descriptions of seismic hazard (Reiter, 1990). After defining the seismic source(s), in the study area, the controlling earthquake is usually selected as the largest earthquake that the seismic source is capable of generating, i.e., the maximum credible earthquake (Reiter, 1990). How the magnitude of the controlling earthquake is defined will determine the level of conservatism of the assessment (Reiter, 1990). The level of ground shaking at the site caused by the controlling earthquake is estimated using a ground motion prediction equation (GMPE) or a numerical method to simulate the ground motion.

For each fault rupture model and GMPE, we compute a set of values of the selected ground motion parameter (e.g., peak ground acceleration and spectral acceleration) for a single site or grid point. We model the earthquake rupture as planar fault segments, using the fault orientation (i.e., strike, dip and rake), the thickness of the seismogenic zone, rupture aspect ratio and a magnitude-length scaling relationship. We do not consider the direction of the rupture and, therefore, the location of the epicenter does not have any effect on the ground motion calculations. Only the location, the dimensions of the fault and the style of faulting are important for the deterministic scenarios. The GMPEs used in this study are derived from large worldwide strong motion datasets for active shallow crustal regime and are considered appropriate for the Tien Shan (see “Selection of the ground motion models” for further discussion).

For each controlling earthquake, we define a single rupture model, and select one or more GMPEs that are combined in a logic tree. Then, we compute multiple realizations of the ground motion value, each realization sampling the aleatory uncertainty in the GMPEs using Monte Carlo simulations. This procedure allows us to include the aleatory uncertainties in GMPEs by selecting the ground motion values from their probability density functions, as defined by the median prediction within one standard deviation (the aleatory uncertainty in the GMPE), which corresponds to the 84th percentile ground motion (e.g., Abrahamson, 2006). This procedure is similar to the scenario-based seismic hazard analysis implemented in the software OpenQuake (e.g., Pagani et al., 2014).

DEFINING THE SCENARIO EARTHQUAKES

In this study, we use the DSHA to estimate ground motion scenarios for the three largest earthquakes recorded in the Northern Tien Shan region between the end of the 19^{th} century and the beginning of the 20^{th} century: the 1887 Ms 7.3 Verny earthquake, the 1889 Ms 8.3 Chilik earthquake, and the 1911 Ms 8.0 Chon-Kemin earthquake (Figure 1). All of them caused heavy damage in Almaty. We refer to them not as controlling earthquakes, but as scenario earthquakes because there is no conclusive evidence that they are either the closest or the largest potential earthquakes to Almaty due to the short length of the earthquake catalogue in the region (see Appendix A). We cannot rule out the occurrence of a destructive earthquake of Mw ≥ 8.0 before 1875, since the earthquake catalogue for Mw 8.0 and greater is complete.

For these earthquakes, we determine the rupture geometry based on the available information in the literature, geological observations, and earthquake physics. We use the self-consistent empirical relationships of Leonard (2010) to estimate the dimension of the fault rupture using Mw, and Mw to estimate the seismic moment M_0 (Kanamori, 1977; Hanks and Kanamori, 1979).

The parameters of the rupture models for the three scenario earthquakes are summarized in Table 1, together with their uncertainties if available from published sources or estimated from the error propagation. The location of the epicenters and the mapped fault ruptures are shown in Figure 2.

1887 Verny earthquake

The 8 June 1887 Verny earthquake was the closest event to Almaty among the earthquakes that occurred between the end of the 19th and the beginning of the 20th century. The epicenter was located ~30 km west of the city. One month after the event, an expedition was sent from St. Petersburg into the epicentral area to collect macroseismic information (Mushketov, 1890). These macroseismic data were used to infer the surface wave magnitude of M_{LH} 7.3 ± 0.5 (Kondorskaya and Shebalin, 1982) (see Appendix A for the definition of M_{LH}). M_{LH} and Ms are almost identical for $M_{LH} \geq 5.4$ (Scordilis, 2006; Bormann et al., 2013). Kondorskaya and Shebalin (1982) also use the macroseismic data to estimate isoseismals, a hypocentral depth of 20 km, and an epicentral intensity I_0 of IX-X ± 0.5 for the Verny earthquake (the intensity scale is not indicated in Kondorskaya and Shebalin, 1982). Tatevossian (2007) estimate a magnitude between M_{LH} 7.3 and 7.5. Using the conversion equation of Scordilis (2006), Ms 7.3 corresponds to Mw 7.3 ± 0.2 (Table 1).

No surface rupture has been identified for this earthquake because the event triggered many large landslides that may have covered the fault trace (Abdrakhmatov et al., 2016). For this reason, very little is known about the rupture process of this event. Using the length-magnitude scaling relationships of Leonard (2010), an earthquake of Mw 7.3 ± 0.2 generates a 75 ± 20 km long and 31 ± 8 km wide rupture (Table 1).

We assume a reverse faulting mechanism with a small strike-slip component, similar to the mechanism of the 1911 earthquake (see Table 1). However, a pure reverse focal mechanism, in agreement with the focal mechanisms determined for other earthquakes in the Zailisky Alatau range, cannot be ruled out.

1889 Chilik earthquake

The 11 July 1889 Ms 8.3 Chilik earthquake is one of the largest historical continental events in the world and one of the earliest teleseismically recorded earthquakes (Krüger et al., 2016). Despite its size, relatively little is known about the source of the earthquake because the isoseismals were the result of the sparse intensity observations in Mushketov (1891). Mushketov (1891) do not report any primary surface rupture and assign a MSK-64 intensity of IX-X around the Chilik River and VII-VIII in Almaty (Figure 3). Kondorskaya and Shebalin (1982) estimate M_{LH} 8.3 based on macroseismic observations. Bindi et al. (2014) determine Ms 8.3 using data from the earthquake catalogue of Mikhailova et al. (2015). Krüger et al. (2016) estimate the event to be between Mw 8.0 and 8.3 with a preferred value of Mw 8.0 by analyzing a fragment of an early Rebeur-Paschwitz seismogram, recorded in Wilhelmshaven, Germany, and magnetograph readings for the earthquake. In this study, we assume the magnitude for this earthquake to be Mw 8.2, which is an average value between the findings of Krüger et al. (2016) and Bindi et al. (2014), with an uncertainty of 0.2 magnitude unit, i.e., the standard deviation in the magnitude conversion equations of Scordilis (2006) (Table 1 and Appendix A). The Chilik earthquake was associated with the E-W trending left-lateral Chon-Kemin-Chilik fault zone (e.g., Abdrakhmatov et al., 2002; 2016; Krüger et al., 2016). The epicentral location is not well constrained by the sparse intensity observations of Mushketov (1891) and the epicentral coordinates have an uncertainty of 0.5º (Kondorskaya and Shebalin, 1982; Bindi et al., 2014).

Recent field investigations have found evidence of fresh scarps that may be associated with the Chilik earthquake (e.g., Tibaldi et al., 1997; Abdrakhmatov et al, 2016). Abdrakhmatov et al. (2016) identify three segments that potentially ruptured during this event: the 45-km-long right-lateral Beshkaragai segment; the 30-km-long Saty segment with an oblique left-lateral slip; and the 100-km-long right-lateral Kurmentey segment (Figure 2). They sum up to a total of 175 km of complex multi-segmented surface rupture including step-overs (up to 6-7 km) (Abdrakhmatov et al., 2016). Using the rupture length-magnitude scaling relationships of Leonard (2010), an earthquake of Mw 8.2 ± 0.2 would be associated with a 260 ± 71 km long rupture. This is longer than the ~180 km surface rupture mapped by Abdrakhmatov et al. (2016). The difference may be explained by: 1) a large hypocentral depth that did not allow the entire fault rupture to reach the surface; or 2) the fact that not all the surface ruptures have been identified (Abdrakhmatov et al., 2016; Krüger et al., 2016).

The hypocentral depth of this seismic event cannot be constrained by the available data. Bindi et al. (2014) and Krüger et al. (2016) suggest a hypocentral depth in the mid or lower crust and a depth of 40 km may be consistent with the isoseismals of this earthquake and the lack of local intensity greater than MSK X (Figure 3). The 24 March 1978 Mw 6.9

Dzhalanash-Tyup earthquake occurred in the epicentral area of the 1889 earthquake and had a hypocentral depth of 35 km. This seems to support the possibility of large hypocentral depth for the 1889 event (Krüger et al., 2016; Abdrakhmatov et al, 2016). However, this hypothesis is not supported by any geological evidence and a depth of 20-25 km cannot be ruled out (Krüger et al., 2016; Sloan et al., 2011).

Since the hypocentral depth is unconstrained, the down-dip width of the rupture is unknown. However, we fix the vertical extent of the fault plane to 40 km, based on Sloan et al. (2011), who suggest that the seismogenic layer is 40 km thick (see "Seismicity in the Northern Tien Shan"). We did not use the scaling relationship of Leonard (2010) to evaluate the down-dip width of the fault rupture because the thickness of the seismogenic layer limits the rupture width, especially for large strike-slip earthquakes (e.g., Leonard, 2010). The focal mechanism of the 1889 earthquake determined from the geomorphological study of Abdrakhmatov et al. (2016) favors oblique-reverse faulting with a large left-lateral strike-slip component. In the rupture model, we assume a dip of 70° (Table 1).

1911 Chon-Kemin earthquake

The 3 January 1911 Ms 8.0 Chon-Kemin earthquake caused less than 500 casualties, considering its size (Bogdanovich et al., 1914; Delvaux et al., 2001). This is because the region mainly affected by this event was the Alatau mountain ranges between Lake Issyk-Kul and Almaty (e.g., Delvaux et al., 2001), which was sparsely populated at the beginning of the 20th century (e.g., Abdrakhmatov et al., 2002; Kulikova and Krüger, 2015). A field expedition was sent to the epicentral area three months after the event to investigate the damage from the earthquake (Bogdanovich et al., 1914). From their observations, Bogdanovich et al. (1914) assign an MSK-64 intensity of X in the epicentral zone and VIII in Almaty (Figure 3).

The earthquake has been studied by various authors, resulting in a number of different estimates of the epicenter and magnitude. Abdrakhmatov et al. (2002) report Ms 8.2. Arrowsmith et al. (2016) infer Mw 7.9 from geological observations. Kulikova and Krüger (2015) estimate the source parameters of the Chon-Kemin earthquake using digitized data from 23 stations worldwide. They compute Mw 8.0 ± 0.1 that we use in the present work.

Bogdanovich et al. (1914) estimate that the epicenter was situated near the junction between the Chon-Kemin, Chilik and Chon-Aksu valleys (Figure 2). Various historical catalogues (e.g., Gutenberg and Richter, 1954; Kondorskaya and Shebalin, 1977) report different epicentral locations whose differences are within 1° in longitude and <1° in latitude (Kulikova and Krüger, 2015).

The Chon-Kemin earthquake produced a total of 145 to 195 km surface rupture on six different segments of the Chon-Kemin-Chilik fault (e.g., Molnar and Ghose, 2000; Abdrakhmatov et al., 2002; 2016; Kulikova and Krüger, 2015). Applying the scaling relationships of Leonard (2010), we estimate that an earthquake of Mw 8.0 ± 0.1 generates a rupture of 202 ± 28 km length. We fix the vertical extent of the Chon-Kemin fault plane to 40 km following the same reasoning as described for the Chilik earthquake. However, it is worth noting that the hypocentral depth of the Chon-Kemin event is 20 ± 3 km (Kulikova and Krüger, 2015), and not 40 km as for the Chilik event. This means that although the two earthquakes have the same vertical fault extent, the 1911 earthquake hypocenter is shallower. This is supported by the trend of the isoseismals that are broader for the 1889 earthquake than for the 1911 earthquake, indicating that the hypocenter may be deeper in the first case (Figure 3).

The Chon-Kemin event was identified as a reverse-faulting event by Molnar and Ghose (2000) because the Chon-Kemin-Chilik fault system was initially interpreted to be a reverse fault system, but other studies have suggested varying amounts of strike-slip movement in addition to the shortening. For example, Kulikova and Krüger (2015) determine a reverse faulting focal mechanism with a minor strike-slip component for the Chon-Kemin earthquake. A significant left-lateral strike-slip component was found by Delvaux et al. (2001) on the Chon-Kemin-Chilik fault segments from field surveys and examination of remote sensing imagery. Arrowsmith et al. (2016) find a complex multi-segmented fault rupture consisting of south-dipping segments in the west and north-dipping segments in the central and eastern part of the fault rupture, with a variable dip angle between 45° and 60°, but with little evidence for strike-slip. In the rupture model of the 1911 earthquake, we use the focal mechanism determined by Kulikova and Krüger (2015), i.e., 264 ± 20° strike, 52 ± 10° dip, and 98 ± 10° rake (Table 1).

Although the studies of Arrowsmith et al. (2016) for the 1911 earthquake and Abdrakhmatov et al. (2016) for the 1889 earthquake show evidence of multi-segmented ruptures with step-overs, we use simplified rupture models (Figure 2). Using the mapped fault traces by Arrowsmith et al. (2016) for the 1911 earthquake and Abdrakhmatov et al. (2016) for the 1889 earthquake would not increase the maximum ground shaking in the earthquake scenarios within one standard deviation. The comparison between our rupture model and the potential mapped segments for the 1889 Chilik earthquake shows some differences (Figures 2 and 3). In order to match the observed intensity distribution (Figure 3), our rupture model was extended further NE than the surface ruptures mapped in Abdrakhmatov et al. (2016). Although no surface ruptures have been reported, the NE extension does follow a Quaternary fault scarp. The potential existence of a rupture on the NE scarps means that either the surface effects have been eroded, or the rupture did not reach the earth's surface.

SELECTION OF THE GROUND MOTION MODELS

The choice of an appropriate GMPE for predicting strong ground motion as a function of magnitude and distance is one of the most difficult aspects of probabilistic and deterministic seismic hazard studies. This is because the hazard estimates are strongly affected by the selected GMPEs, both in terms of expected median prediction and aleatory uncertainty. It is generally considered good practice in seismic hazard assessment to try to account for epistemic uncertainty (i.e., the lack of knowledge about which model is best to adopt) by combining different GMPEs in a weighted logic tree (e.g., Frankel et al., 2002; IAEA, 2010).

We adopt the GMPE exclusion criteria of Bommer et al. (2010) to select the most appropriate GMPEs for our study. The first criterion excludes GMPEs that are not relevant to this tectonic regime. The rest relate to the ground motion parameters, the magnitude-distance range covered by the GMPE, and its functional form. By identifying a set of appropriate GMPEs, we can take into account the epistemic uncertainties in the ground motion models.

The Northern Tien Shan is considered an active shallow continental regime (ASCR). We use three GMPEs that have been developed for crustal earthquakes in other ASCRs using a worldwide dataset of ground motion recordings. These models are Boore et al. (2014), Chiou and Youngs (2014), and Akkar et al. (2014). The models of Boore et al. (2014) and Chiou and Youngs (2014) are two GMPEs from the ‘Next Generation Attenuation - West2’ project (Bozorgnia et al., 2014), whose GMPEs were derived from a large database of strong motion recordings of earthquakes worldwide. The model of Akkar et al. (2014) is derived from the ground motion recording dataset of Europe and the Middle East. The chosen GMPEs are combined in a logic tree and the weights assigned are 0.35 for Boore et al. (2014), 0.35 for Chiou and Youngs (2014), and 0.30 Akkar et al. (2014). Earlier versions of these GMPEs have been compared with the unpublished dataset of the ground motion recordings of the

Institute of Seismology in Almaty (N. Silacheva, personal comm., 2015) and found to have an acceptable agreement with the local ground motion recordings within one standard deviation. In this work, we selected the updated GMPE for Akkar and Bommer (2010), Boore and Atkinson (2008), and Chiou and Youngs (2008) because one of the exclusion criteria of Bommer et al. (2010) proposes to exclude the models that have been superseded by more recent publications.

We also estimate the earthquake scenario in terms of intensity, using two intensity prediction equations (IPE): Bindi et al. (2011), as modified by Ullah et al. (2015); and Allen et al. (2012). The IPE of Bindi et al. (2011) was derived from 66 earthquakes in Central Asia with magnitudes between Ms 4.6 and 8.3 and it is expressed in terms of the MSK-64 scale. The primary distance metric is epicentral distance and therefore it does not account for the finite extent of the fault rupture. The intensity model of Allen et al. (2012) is derived from a large worldwide dataset of > 13,000 crustal earthquakes from Mw 5.0 to 7.9. This uses the closest distance to rupture, therefore accounting for the finite dimensions of the fault rupture. We assigned a weight of 0.5 to each IPE.

We assume a rock site condition and, therefore, the time-averaged shear wave velocity of the top 30 m of material (v_{s30}) is 760 m/s for the hazard calculations.

HAZARD CALCULATIONS

Using a DSHA approach and the rupture models described above, we generated 1000 ground motion scenarios for each scenario earthquake to account for the aleatory uncertainties in the GMPEs. Then, we calculated the mean and the standard deviation of the 1000 deterministic ground motion values. We found that this number of iterations provides a clear convergence towards stable average and standard deviation. In the simulations of the earthquake scenarios, we did not account for the uncertainty in the parameters of the fault rupture models and therefore the fault rupture model is the same for all scenarios. We perform a sensitivity analysis to test the influence of the parameters of the fault rupture models on the deterministic scenarios.

In this section, we show the ground motion scenarios for peak ground acceleration (PGA) (Figure 4) and MSK-64 intensity (Figure 5) on a regular 0.05X0.05° grid for the 1887 Verny, 1889 Chilik, and 1911 Chon-Kemin earthquakes. The distributions of the 0.2 s and 1.0 s spectral acceleration (SA) for the three scenario earthquakes are displayed in Appendix C. The largest PGA values in Almaty are determined for the 1887 earthquake because the city is situated in the surface projection of the fault plane and therefore the Joyner-Boore distance (Rjb) is 0.0 km. The distance between Almaty and the epicenter of the Verny earthquake is 21 km, whereas the distance between Almaty and the epicenter of the Chilik and Chon-Kemin earthquakes was 134 and 63 km, respectively (Table 2).

The distribution of the standard deviation for the MSK-64 intensity is uniform within the grid area and is up to MSK I. The intensities in the epicentral area and in Almaty (Figure 5) agree well with the isoseismals in Figure 3. For the 1911 earthquake, we estimated an intensity of IX ± I in the epicentral area and VIII ± I in Almaty; whereas, the isoseismals of Bogdanovich et al. (1914) report an intensity of X in the epicentral area and VIII in Almaty. For the 1889 earthquake, Mushketov (1891) estimate an intensity of IX-X around the Chilik River and VII-VIII in Almaty; and our calculations show an intensity of IX ± I around the epicenter and VIII ± I in Almaty.

Table 3 shows the mean values of PGA, 0.2 s SA, 1.0 s SA, and MSK-64 intensity for the three scenario earthquakes for a central location in Almaty situated at 43.28°N and 76.90°E. The PGA value for the 1911 Chon-Kemin event is 0.23 ± 0.08 g, the 0.2 s SA is 0.48 ± 0.17 g, the 1.0 s SA is 0.17 ± 0.07 g, and the MSK-64 intensity is VIII ± I. Clearly, these estimates are associated with large uncertainties and the standard deviations are relatively high, due to the large uncertainty in the GMPEs. The values of the MSK-64 intensity for the three earthquakes are identical because the intensity is rounded to the nearest integer.

To check which input parameters have the strongest influence on the earthquake scenarios, we made a sensitivity analysis at the site in Almaty, using the 1911 Chon-Kemin earthquake. We performed seven tests for the sensitivity analysis. In each test, we changed one parameter from the rupture model in Table 1, referred as to reference model, and kept the other parameters constant. The parameters tested include moment magnitude, fault dimensions, site condition, GMPEs, and fault plane orientation. For each test, we generated 1000 ground motion scenarios and computed their mean and standard deviation (Table 4). Most of the tests produce similar results within one standard deviation. When we use only one GMPE (Tests 2, 3, and 4), the deterministic ground motion values are relatively consistent with each other. The dip angle in the fault rupture model of the scenario earthquake has a strong influence on the deterministic scenarios, as shown by the deterministic values for Tests 5 and 6. It is worth noting that Test 7 considers a multi-segmented fault rupture. It consists of four segments: from west to east, a 45° south-dipping segment, two 60° north-dipping segments, and a 45° north-dipping segment. The ground motion parameters obtained for Test 7 are smaller than the values computed for the reference model, but still within the uncertainty. This is because the fault segment closer to the site has a larger dip angle (dip=60°) in Test 7 than in the reference model (dip=52°) and therefore the surface projection of the fault plane is further from Almaty than in the reference model. For this reason, the ground shaking felt in Almaty is lower.

Probabilistic approach

In this section, we take the results from the Hazard Calculations section for DSHA and determine the exceedance frequencies for the ground motions computed for the scenario earthquakes, using PSHA. A probabilistic approach to seismic hazard assessment combines seismological, geological and geophysical data to produce a probabilistic description of the distribution of future shaking that may occur at a site (e.g., Reiter, 1990; McGuire, 2004).

We perform a PSHA using the Monte Carlo-based simulations developed by Musson (2000). The site for which the hazard is calculated is the same as in the scenario modeling. The source zone model used in the computation is based on the earthquake catalogue (see Appendix A), tectonics, geology, and kinematic constraints in the Northern Tien Shan. Using this model and Monte Carlo simulations, we generate 100,000 synthetic earthquake catalogues, each 100 years long. This gives a total of 10,000,000 years of simulated data that is sufficient to resolve the hazard accurately for long return periods (Musson, 2000). Each simulated catalogue represents a version of what could occur based on observed seismicity. The ground motion is computed for each earthquake in the simulated catalogues. Then, by sorting the ground motion results in order of decreasing severity, it is possible to identify ground motions associated with different frequencies of exceedance (Musson, 2000).

The second stage of the probabilistic hazard analysis involves disaggregating the hazard results in terms of magnitude, distance, and epsilon (ε, the number of standard deviations above or below the median prediction). We do this in order to determine whether earthquakes similar to the scenario earthquakes considered in the DSHA dominate the ground motion hazard at the site. In our approach, this simply means searching the synthetic catalogues derived from the source model for ground motions that are greater than or equal to the deterministic ground motion values within the standard deviation (Musson, 2000).

SEISMIC SOURCE ZONE MODEL

The study area is divided into a series of seismic sources. Seismic activity in each seismic source is considered to be uniform, and earthquakes have an equal chance of occurring at any point in the zone.

The source model for this work includes the Northern Tien Shan and the South Kazakh Platform because other tectonic structures, such as the Tarim Basin, are at distances more than 400 km from Almaty to be considered relevant to the hazard at the site. The model is based on seismological, tectonic and geological analysis of the region and consists of 16 zones and two faults (Figure 6). All zones are terminated arbitrarily at the edge of a 400-km radius circle centered in Almaty. We grouped the source zones into larger units where similar tectonic constraints can be applied. The tectonic units are the Western Tien Shan, which is separated by the Northern Tien Shan by the Talas-Ferghana fault; the upper Northern Tien Shan and the lower Northern Tien Shan; the Tien Shan Foreland; the Eastern Tien Shan; and the Kazakh Platform. The Northern Tien Shan is divided into two tectonic groups because the upper Northern Tien Shan has higher seismic activity than the lower Northern Tien Shan in terms of magnitude and frequency.

The faults included in the source model are the Chon-Kemin-Chilik fault system (fault source CKCF) and the Talas-Ferghana fault (fault source TFF). We did not include any other fault systems (e.g., Fore-Terskey fault to the south of Lake Issyl-Kul, and the Atushi-Keping fault between the Tien Shan and the Tarim Basin) because the information on their geometry, the rupture behavior, and the maximum magnitude they are capable of generating is incomplete or unknown. Furthermore, although the overall deformation rate of the Tien Shan mountain belt is known, it is difficult to partition it among the active tectonic structures in the region and thus estimate the activity rate of the individual faults. This is because earthquakes are distributed over fault zones of hundreds of kilometers in width, on complex networks of many, highly segmented faults, each accumulating slip at a few tenths to a few millimeters per year (England and Jackson, 2011; Liu and Stein, 2016). In the approach we used for PSHA, each simulated earthquake in the source zones is located at the center of a finite fault rupture. The size of the rupture is computed using the magnitude of the synthetic event, the magnitude-length scaling relationship of Leonard (2010), the fault orientation, and the faulting style. Using this procedure, faults are taken into account in general. One of the advantages of this approach is to reduce the likelihood of neglecting important but unknown tectonic structures.

We modeled the Chon-Kemin-Chilik fault system as an individual fault in the source model because the 1889 and 1911 earthquakes were generated along it. Its slip rate was estimated using both the seismic moment tensors of the major earthquakes in the 20th century (Molnar and Deng, 1984; Molnar and Ghose, 2000) and GPS data (e.g., Abdrakhmatov et al., 1996; Zubovich et al., 2010). Furthermore, its geometry is known from the recent geomorphological studies (Delvaux et al., 2001; Arrowsmith et al., 2016; Abdrakhmatov et al., 2016). Since no earthquakes of Mw 7.0 have occurred along TFF in the last 200 years, it is not straightforward to quantify the maximum magnitude it can generate. However, we decided to model it as an individual fault in the source model because it is a major tectonic structure in the Northern Tien Shan. Zubovich et al. (2010) estimate an annual slip rate of less than 2 mm/yr based on geodetic data from a dense, regional GPS network (see “Recurrence statistics” for further discussion).

Recurrence statistics

We applied the truncated Gutenberg-Richter law (Gutenberg and Richter, 1954) to the individual zones of the source model using the penalized maximum likelihood procedure (Johnston et al., 1994), the earthquake catalogue and its completeness analysis in Appendix A, and the best regional estimate $b = 0.96$ as a weighted prior for each of the zones (see Appendix B). Below we describe in detail the recurrence statistics for zone NISK (the North Issyk-Kul region) because it contains the three scenario earthquakes used in the DSHA described earlier. The results of the recurrence statistics for all zones of the source model are displayed in Appendix B.

The best-fit values of NISK are N (≥ Mw 4.5) = 0.90 ± 0.13 and $b = 0.826 \pm 0.078$ (Figure 7). The error-bars in Figure 7 are inversely proportional to the number of observations above a certain magnitude in the catalogue and describe the uncertainties in the long-term recurrence for that magnitude value. The recurrence parameters suggest an earthquake somewhere in NISK with a magnitude of Mw 8.0 or above every 864 ± 438 yr. The observed rate for earthquakes of Mw ≥ 7.0 seldom matches the predicted seismicity by the Gutenberg-Richter law because a 100-year sample of seismicity may contain by chance an earthquake with a recurrence of 1000 years. This is especially true for intraplate areas, such as the Tien Shan, where the 138-yr long earthquake catalogue is shorter than the potential recurrence interval of the large earthquakes (e.g., Abdrakhmatov et al., 2016; Landgraf et al., 2016a). The occurrence of two earthquakes with magnitudes higher than Mw 8.0 in 20 years (i.e., the Chilik earthquake in 1889 and the Chon-Kemin earthquake in 1911) can be explained by the fact that large intraplate earthquakes occur on faults that remain dormant for a long time and become active for a short period interacting with neighboring tectonic structures (e.g., Landgraf et al., 2016b). Therefore, the recurrence interval of these seismic events is less regular than the recurrence interval of earthquakes at plate boundaries (e.g., Liu and Stein, 2016). To model the deficit of predicted seismicity for Mw ≥ 7.0 in Figure 7, we treat the seismicity of NISK as two populations of earthquakes predicted by the truncated Gutenberg-Richter law: a population of "normal" activity represented by the levels of seismicity in the range Mw 4.5 to 6.9, and a second population consisting of earthquakes in the range Mw 7.0 to 8.5. This procedure avoids underestimating the seismicity for earthquakes of Mw ≥ 7.0 (Figure 7). In PSHA this can be handled by modeling the source zone twice with the same geometry for each earthquake population (Musson and Sargeant, 2007; Musson, 2015). The best-fit values for the population of earthquakes in the range Mw 7.0 to 8.5 are N (≥ Mw 4.5) = 2.58 ± 2.24 and b = 0.793 ± 0.098. This suggests an earthquake of Mw 8.0 and above somewhere in NISK every 231 ± 262 yr.

We estimated the activity rate of the fault sources from their annual slip rate, using the relationship of Youngs and Coppersmith (1985) (see Appendix B). For the fault source CKCF, we used an annual slip rate between 0.1 and 3.0 mm/yr (Thompson et al., 2002) and b = 0.826 ± 0.078 of NISK). We computed an activity rate of N (≥ Mw 4.5) = 0.14 ± 0.10 (see Appendix B for further information). This is equivalent to an earthquake of Mw 8.0 and greater every 5557 ± 2148 yr. For the fault source TFF, we used a range between 0.1 and 1.5 mm/yr for the annual slip rate (Zubovich et al., 2010) and the b-value of the entire study area, b = 0.959 ± 0.020 that is similar to the b-value of the neighboring source zones. The activity rate for TFF is N (≥ Mw 4.5) = 0.135 ± 0.092 suggesting an earthquake of Mw ≥ 8.0 every 16168 ± 16610 yr.

The recurrence statistics described in this section highlights the limitations in estimating reliable earthquake rates in regions where the length of the seismic record is shorter than the average recurrence interval of the largest earthquakes (here 231 ± 262 yr. for an earthquake of Mw > 8.0). This explains also why the standard deviation of the recurrence intervals is very large, up to the same order of the value itself (i.e., 5557 ± 2148 yr. for CKCF and 16168 ± 16610 yr. for TFF).

Maximum magnitudes

Maximum magnitude (Mmax) is the largest possible earthquake that is considered in the hazard analysis. This is often highly uncertain, although, in a broad sense, the maximum magnitude can be constrained by fault length because any large earthquake requires a sufficiently large structure to host it. However, this approach is challenging in low strain continental interiors, including the Tien Shan, for the following reasons. First, faults in continental interiors are spread over a large region and are usually extensively segmented (e.g., England and Jackson, 2011). Some of these fault segments are unknown or poorly constrained before an earthquake occurs along them (e.g., Landgraf et al., 2016a; Grützner et al., 2017). Second, due to the low strain accumulation on the faults, the recurrence interval of large earthquakes is of the order of thousands of years. Therefore, the instrumental and historical records of seismicity probably do not include the largest possible earthquakes (e.g., Abdrakhmatov et al., 2016; Landgraf et al., 2016a). This is especially true for the Northern Tien Shan where the earthquake catalogue is 138 years long. For this reason, a realistic assessment of the uncertainty in Mmax should allow for the possibility of significantly larger events in the future. The distribution of Mmax for the source zones and the fault sources of the source model is assigned on the basis of the tectonic groups and is given in Table 5.

Ullah et al. (2015) assign a maximum magnitude of Mw 8.3 to their Northern Tien Shan zone, which includes our zone NISK, and therefore contains the Mw 8.0 Chon-Kemin earthquake and the Mw 8.2 Chilik earthquake. A single value for Mmax is inappropriate for NISK considering the short length of the earthquake catalogue in the Tien Shan. We used three values of Mmax for NISK (i.e., Mw 8.2, 8.3 and 8.5) with a weight of 0.40, 0.40, and 0.20, respectively (Table 5).

HAZARD CALCULATIONS

Using a Monte Carlo-based PSHA and the source model described above, we simulated 100,000 earthquake catalogues, each 100 years long. The ground motion at the site for each simulation was estimated using the logic tree previously discussed. We did not apply any ground motion truncation for the GMPEs in the hazard calculations for PSHA.

The results are expressed as hazard curves that show the annual frequency of exceedance as a function of PGA, 0.2 s, and 1.0 s SA and MSK-64 intensity for the site in Almaty situated at 43.28°N and 76.90°E (Figure 8). The return periods (i.e., the inverse of the annual frequency of exceedance) corresponding to the ground motion values simulated for DSHA in Table 3 are obtained by interpolation from the hazard curves in Figure 8 and shown in Table 6. The return periods are associated with large standard deviation because the large variability of the ground motion values propagates into larger uncertainties in the return period. For the MSK-64 intensity, the standard deviation of the return period is larger than the return period itself. For a return period of 10,000 years, the ground motion values are PGA=1.34 g, 0.2 s SA=2.06 g, 1.0 s SA=1.13 g and MSK-64 =X. In Figure 8, we also show the comparison between the hazard curves estimated for the source model with 16 area zones and two fault sources and the source model with 16 area zones only. This displays clearly that we did not double-count the earthquakes, and therefore over-predict the seismicity in the vicinity of the Chon-Kemin-Chilik fault system, although we estimated the activity rate of area source zones and fault sources independently. It is not surprising that the fault sources, especially CKCF, which is less than 100 km from the site, do not contribute much to the hazard in Almaty. This is because the faults closer to Almaty are more hazardous than CKCF, although they are poorly understood and thus their threat has not been recognized (see Discussion).

It is useful to compare the hazard curves of this study with previous works. Most hazard studies in Central Asia use the intensity as primary ground motion parameter, which is then often converted into PGA (e.g., Ulomov et al., 1999). We compare our hazard curve for the MSK-64 intensity with two studies developed for two worldwide projects: Ulomov et al. (1999) and Ullah et al. (2015). In the Global Seismic Hazard Assessment Program (Giardini, 1999), Ulomov et al. (1999) performed PSHA for Northern Eurasia (30°-90°N and 20°-170°E) and their maps show that the MSK-64 intensity is around IX for 10% probability of exceedance in 50 years in the Northern Tien Shan (Table 7). For the "Earthquake Model for Central Asia" project (Parolai et al., 2015), Ullah et al. (2015) performed PSHA for the whole of Central Asia (i.e., 34°-56°N and 47.5°- 90°E), using the catalogue of Mikhailova et al. (2015) and the GMPE of Bindi et al. (2011). Their maps show an MSK-64 intensity between VII and VIII for a 475-year return period for Almaty (Table 7). We determined an MSK-64 intensity between VIII and IX for a return period of 475 (Table 7). We compare our hazard curve for PGA with the work of Silacheva et al. (2017). They performed a Monte Carlo-based PSHA for Kazakhstan and Almaty using a local catalogue and the GMPEs of Akkar and Bommer (2010), Boore and Atkinson (2008), Campbell and Bozorgnia (2008), Chiou and Youngs (2008), and Zhao et al. (2006). Their maps show that the PGA in Almaty is between 0.36 and 0.44 g for a 475 year return period, whereas we estimated a PGA of 0.44 g in Almaty for the same return period (Table 7). The comparison with Ulomov et al. (1999), Ullah et al. (2015), and Silacheva et al. (2017) is reasonable considering that the four studies are based on different earthquake catalogues, different source models, and different ground motion models. It is worth underlining that a seismic hazard map is intended to be indicative only and will not be expected to give exactly the same results as a site-specific study.

In the second stage of the hazard analysis, we disaggregated the ground motion hazard results for PGA, 0.2 s SA and 1.0s SA in terms of magnitude, Joyner-Boore distance Rjb, ε and the originating source zone to determine which earthquake(s) is most likely to produce the hazard values in Table 6. We performed the disaggregation analysis for the return periods computed for the three scenario earthquakes, but we only show the results for the 1911 and 1887 earthquakes because they seem to influence more the hazard at Almaty. Disaggregating by zone, we see that the largest influence (between 80 and 97%) on the hazard comes from NISK. This is expected because NISK is next to the site and has high levels of seismicity. The overall hazard is dominated by earthquakes at distances less than 30 km from Almaty within the zone NISK because the seismicity is uniformly distributed within the zone and therefore earthquakes have equal chance to occur anywhere in the zone. The disaggregation plots in terms of magnitude, distance and ε are shown in Figure 9 for the PGA and in Appendix C for 0.2 s SA, 1.0 s SA, and MSK-64 intensity. The disaggregation plot in Figure 9a corresponds to return periods of 139 ± 81 yr and shows that the hazard is dominated by earthquakes of Mw 4.8 to 5.0 at distances of Rjb < 10 km. As the return period increases, the dominant contribution is from earthquakes of Mw 7.0 to 7.2 at distances of less than 10 km, but earthquakes of Mw 7.2 to 7.8 at distances between 10 and 30 km contribute to the overall hazard (Figure 9b). Figure 9 clearly suggests that future earthquakes similar to the 1887 Verny earthquake strongly influence the overall seismic hazard of Almaty. However, it is worth noting that the histograms in Figure 9 are very broad because the values for PGA, 0.2 s SA and 1.0 s SA and the corresponding return periods used in the disaggregation analysis are based on the ground motion values, together with their standard deviation, computed by the DSHA.

The disaggregation analysis for a return period of 10,000 years indicates that the earthquakes that dominate the hazard are given by earthquakes at distances less than 10 km from Almaty with magnitudes of Mw 7.6 to 7.8 for PGA.

Discussion

The aim of this paper was to gain new insights into the earthquake hazard of the Northern Tien Shan by using the best available science and combining outcomes from the deterministic and probabilistic approaches. This approach helps overcome our limited understanding of most faults in terms of source geometry, rupture behavior, slip rate, and maximum magnitude and the short length of the earthquake catalogue available in the region.

The deterministic approach for seismic hazard analysis can be considered a special case of PSHA. Therefore, the scenario earthquakes used in DSHA are included in PSHA because the latter considers all possible earthquake scenarios and ground motion levels that occur on the seismic sources affecting the site. The disaggregation analysis is an excellent tool to integrate the results from the two approaches. First, we applied DSHA for the largest earthquakes recorded in the Northern Tien Shan. Then, we used PSHA to determine the chance of exceeding the deterministic ground motion values (Figure 8). The disaggregation plots in Figure 9 and Appendix C tell us whether the scenario earthquakes dominate the overall ground motion hazard of Almaty. They show that the earthquake(s) similar to the 1887 Verny Mw 7.3 earthquake dominate the hazard for the city. However, these plots are associated with large uncertainties due to the large uncertainties in the input parameters propagating into the deterministic ground motion values (Table 3) and the corresponding return periods (Table 6).

Generally speaking, the uncertainties in the hazard results reflect the many limitations of our current knowledge on the occurrence of future earthquakes in the Tien Shan. This is because the hazard results are estimated using incomplete, and sometimes potentially misinterpreted data (e.g., earthquake catalogues and fault mapping data) and models (e.g., geodynamic and tectonic models) that are based on an instrumental earthquake history of a few of hundreds of years in the best case, compared to the geological history that is up to millions of years (e.g., Stein et al., 2012). This issue is particularly important in low strain continental environments where the tectonic loading rates are low. For this reason, we cannot say whether the largest earthquakes in the seismic catalogue are also the controlling earthquakes for Almaty. The impact of a short earthquake catalogue on the seismic hazard analysis is illustrated clearly in Subsection "Recurrence statistics". In this section, we have shown that the 138 years length of the seismic record is much shorter than the average recurrence interval of the largest earthquakes (from several hundred to thousand years for an earthquake of Mw ≥ 8.0). If we consider the recurrence intervals of individual faults, they are even longer, as shown by our recurrence statistics for CKCF and TFF and confirmed by recent paleoseismological studies (e.g., Abdrakhmatov et al., 2016; Landgraf et al., 2016a). For example, Abdrakhmatov et al. (2016) find evidence that the fresh scarp on the Saty fault segment associated with the 1889 Chilik earthquake was the only surface-rupturing event on this fault in the last 5,000 years. Furthermore, the concept of regular recurrence interval may not be applicable to intraplate continental regions where faults are widespread, highly segmented and often poorly mapped, and the tectonic loading of the faults is slow and variable due to the interaction between faults (e.g., Liu and Stein, 2016).

In this context, it is understandable why the source zone NISK controls the hazard and the fault source CKCF does not contribute much to the overall hazard in Almaty. In NISK, faults are taken into account in general to reduce the likelihood of neglecting important but unknown tectonic structures and therefore the seismicity rate of NISK is higher than the seismicity rate of CKCF. The results of the PSHA show clearly that the threat to the city comes from nearby faults that are little understood in terms of their source geometry, rupture behavior, slip rate and maximum expected earthquake magnitude. Although these faults close to Almaty are not long enough to generate earthquakes of Mw ≥ 7.3, they would pose a significant hazard due to their proximity to Almaty (Grützner et al., 2017). For example, Grützner et al. (2017) report that the irrigation canal that diverts water from the River Chilik to the metropolitan area of the city crosses the faults of the Zailisky Alatau Range Front several times.

Integrating the outcomes from DSHA and PSHA may be also a powerful tool for community-based risk reduction activity and earthquake risk management. The development of simple deterministic scenarios for potential future earthquakes, together with their frequency of occurrence, would contribute to translate the effects of earthquakes into real-life impact (ODI, 2016). This is especially important in densely populated areas in continental low strain rate environments, such as Almaty, where the largest recorded earthquakes occurred in historical or prehistorical time and therefore collective memory of those disasters in the population and society reduces with time.

Conclusions

This work has highlighted the importance of integrating the outcomes from PSHA and DSHA to reduce, and possibly overcome, the limited amount of seismological, geological and geodetic data in the Tien Shan mountain belt.

The main finding of the paper is that the major contribution to the seismic hazard of Almaty comes from earthquakes of Mw 7.0 to 7.5 with Rjb < 10 km to the city at return periods smaller than 1000 years. Future earthquakes similar to the 1887 Mw 7.3 Verny earthquake strongly influence the overall ground motion hazard of Almaty. It is important to highlight that these estimates are associated with large uncertainties due to the large uncertainties in the input parameters. Furthermore, the Verny earthquake is the least well characterized of the three destructive historical earthquakes recorded in the Northern Tien Shan between the end of the 19th and the beginning of the 20th century because its rupture process is unknown, making the rupture model in the deterministic scenario hypothetical.

Future research should focus on reducing the uncertainties in the rupture model by mapping the faults in the region, especially around Almaty, searching for evidence of the occurrence of paleo-earthquakes on them and characterizing the source of the Verny earthquake. The assessment of the seismic hazard for Almaty should also include the effects of local site geology that may result in de-amplifying or amplifying the ground motions. These may have a strong impact in regions where urban areas are situated in valleys and depressions, such as Almaty (Pilz et al., 2015). Any new information should then be used to update the assessment of the seismic hazard for Almaty.

Data and Resources

The online database of the International Seismological Centre is at http://www.isc.ac.uk (last accessed November 2016). The earthquake catalogue for the "Earthquake Model for Central Asia" (EMCA) project is at http://www.emca-gem.org/general/tasks/seismic-hazard-and-microzonation/ (last accessed November 2016). All the other data used in this paper came from published sources listed in the references. The plots were made using the Generic

Mapping Tools version 4.5.2 (www.soest.hawaii.edu/gmt; last accessed June 2010; Wessel et al., 2013).

Acknowledgments

This work was funded by the Natural Environmental Research Council under the grant Earthquake without Frontiers EwF_NE/J02001X/1_1. We are grateful to Richard Luckett, Roger Musson, Margarita Segou, and Natalya Silacheva whose insightful comments were helpful in improving the manuscript. We thank the EMCA project for making their earthquake catalogue freely available. We also thank the reviewers and the Editor Ivan Wong for their constructive comments that contributed significantly to improve the manuscript. This work is published with the permission of the Executive Director of the British Geological Survey.

Appendix A

The earthquake catalogue of this work contains data from three sources: the International Seismological Centre Bulletin (ISC); the World Seismicity Database (WSD) of the British Geological Survey (Henni et al., 1998); and the earthquake catalogue for the “Earthquake Model for Central Asia” (EMCA) project (Mikhailova et al., 2015). The ISC Bulletin is generally regarded as a definitive record of the Earth's instrumental seismicity and contains data from 1900 to the present. The WSD contains parametric data for earthquakes from 2500 BC onwards and has been compiled over a period of thirty years from various catalogues (Henni et al., 1998). The earthquake catalogue for the EMCA project includes information for 33620 earthquakes that occurred in Central Asia in the period from 2000 BC to 2009 AD, although most of the entries (i.e., 33378) are for earthquakes that occurred after 1900 (Mikhailova et al., 2015).

It is standard practice in seismic hazard assessment to use moment magnitude (Mw; Bolt and Abrahamson, 2003). However, these three catalogues contain magnitude estimates in different magnitude scales. Therefore, we converted the magnitude estimates to Mw using the equations of Scordilis (2006), which are based on a large global dataset of earthquakes and includes data from various tectonic regimes. This is one example that illustrates the conversion process we used. The ISC catalogue contains a number of different magnitude estimates for each earthquake determined by different agencies that reported the event (e.g., surface-wave magnitude Ms, body-wave magnitude mb, Mw). We used the hierarchy in Table A.1 to select one magnitude from the available estimates. The list of agencies is the result of a careful application of a decision-making process, together with the reliability of the agency in the magnitude determination. Similarly, we apply a hierarchical approach to the WSD data because they also contain different magnitude estimates determined by different agencies.

The EMCA catalogue merges many sources and magnitude scales. The magnitude of this catalogue is the surface wave magnitude M_{LH} that is widely used in former Soviet countries and based on the Moscow-Prague formula (Karnik, 1962; Bormann et al., 2013). The original magnitude of the earthquakes in the EMCA catalogue is not indicated (Mikhailova et al., 2015; Ullah et al., 2015). We used only events with magnitudes $M_{LH} \geq 5.4$ from the EMCA catalogue if they were not included in the ISC and WSD database. The reason for this is that the uncertainty in the magnitude conversion $M_{original} \rightarrow M_{LH} \rightarrow Mw$ becomes large for $M_{LH} < 5.4$ and may produce an overestimation in the final Mw value (Scordilis, 2006).

DECLUSTERING AND COMPLETENESS

To decluster the earthquake catalogue and therefore to remove the dependent events (aftershocks and foreshocks) from the catalogue, we use the approach of Musson (2000), which is a modified version of the moving window method of Reasenberg (1985). The procedure for declustering the catalogue shows that the most appropriate window in time and space has a length of 30 days and 30 km, respectively. If an earthquake is identified as a mainshock, all events within 30 km of the epicenter and 30 days before and after that event are considered to be dependent events.

To assess the completeness of the catalogue as a function of time, we use the statistical approach of Stepp (1972), modified by Musson (2000). This is based on estimates of the mean seismicity rate of earthquakes for different magnitude ranges and time windows. Our analysis suggests that the catalogue is complete for magnitudes > Mw 4.5since the second half of the twentieth century (Table A.2). This estimate corresponds to the deployment of the World-Wide Standardized Seismographic Network in the early 1960s. The historical record of seismicity in the Tien Shan is relatively short and, even for events of ≥ Mw 7, is probably complete only since the 1880s when the construction of Russian fortresses started in the region (Molnar and Deng, 1984; Korjenkov et al., 2003). The magnitude thresholds in Table A.2 agree with the completeness analysis of the EMCA earthquake catalogue for ≥ Mw 5.5, but our completeness analysis is more conservative for smaller magnitudes.

Appendix B

RECURRENCE STATISTICS

To determine the frequency of occurrence for the seismicity in the Northern Tien Shan, we use the Gutenberg-Richter recurrence law, i.e., the relationship between the magnitude and number of earthquakes in a given region and time period (Gutenberg and Richter, 1954):

$$\text{Log } N = a - b \text{ M} \quad (1B)$$

where N is the number of earthquakes above a given magnitude M. The activity rate, *a,* describes the total number of earthquakes per year above M 0.0 in the study area, and the *b*-value gives the proportion of large events to small ones. In general, *b*-values tend to be close to one (e.g., Reiter, 1990).

We determine the recurrence parameters *a* and *b* for the earthquake catalogue using a penalized maximum likelihood procedure (Johnston et al., 1994). This procedure uses the truncated Gutenberg-Richter recurrence law where the earthquake magnitudes are bounded by lower and upper bounds:

$$N(M) = 10^{a(Mmin)} \frac{e^{-\beta(M-Mmin)} - e^{-\beta(Mmax-Mmin)}}{1-e^{-\beta(Mmax-Mmin)}} \quad (2B)$$

where $\beta = bxln(10)$, M_{min} = minimum magnitude and M_{max} = maximum magnitude. This method considers different time windows of the catalogue for the magnitude completeness thresholds, the correlation between *a* and *b*, and a weighted prior constraining the *b*-value when there are few earthquakes in the source zone for a realistic estimate. The recurrence parameters are computed in terms of *pdf*s and therefore it is straightforward to estimate their uncertainties. We used a correction factor in the activity rate calculations based on the standard error of individual earthquake magnitudes, as proposed by Rhoades and Dowrick (2000). This is because ignoring uncertainty in the magnitude values results in an overestimation of the activity rate (e.g., Rhoades and Dowrick, 2000; Castellaro et al., 2006). We assume that all magnitude values in the catalogue have an uncertainty of ± 0.2 that corresponds to the standard deviation in the magnitude conversion equations of Scordilis (2006). This uncertainty may be too small for historical events in the Tien Shan, as suggested by Zöller at al. (2017) who use $\sigma = \pm 0.5$ for historical events, $\sigma = \pm 0.25$ for early instrumental events and σ = ± 0.1 for recent instrumentally recorded events in Central Asia. However, we decided not to use these values since it is not clear from how these have been estimated. Musson (2012) shows that the magnitude uncertainty should be used carefully to avoid over- or under-estimation of the activity rate in the area under investigation, especially when the earthquake catalogue merges many sources and contains more than one original magnitude scale, as the case of the catalogue in this study.

Equation (2B) was applied to all the seismicity in the study area, using the maximum likelihood method and the completeness thresholds in Table A.2. The best- fit values for equation (2B) are N (Mw $\geq$ 4.5) = 28.19 ± 0.72 and b = 0.959 ± 0.020 (Figure B.1). The predicted seismicity from the Gutenberg-Richter relationship fits the observed rates of seismicity well. The error-bars in Figure B.1 are inversely proportional to the number of observations above a certain magnitude in the catalogue and, therefore, describe the uncertainties in the long-term recurrence for that magnitude value.

Mikhailova et al. (2015) have found a *b*-value of 0.805 for the whole of Central Asia (i.e., 34°-56°N, and 47.5°- 90°E), which is smaller than the estimated *b*-value in this work. The difference between the two values may be explained by three reasons. First, we applied equation (2B) to a smaller region (i.e., 39°-46°N and 70°-81°E) than the whole of Central Asia. Second, the earthquakes in our catalogue are expressed in Mw, and not in M_{LH} as in the earthquake catalogue of Mikhailova et al. (2015). Therefore, different magnitude conversion equations were applied to homogenize the two catalogues. Third, the completeness analysis of the two catalogues is different for Mw < 5.5 (see Appendix A).

The best regional estimate for *b* of 0.96 was used as a weighted prior for the individual zones of the source model (see the “Recurrence Statistics” Subsection). Using equation (2B) and the completeness values in Table A.2 we determined the recurrence parameters *a* and *b* for the individual source zones (Figure B.2 and Table B.1).

We estimated the activity rate of the fault sources from their annual slip rate, using the relationship of Youngs and Coppersmith (1985):

$$N(M) = \frac{\mu AS\,(d-b)\{1-e^{[-\beta(Mmax-M)]}\}}{bM_o^{max}e^{\{-\beta(Mmax-M)\}}} \qquad (3B)$$

where *N* is the number of earthquakes above a given magnitude *M*, *S* is the annual slip rate, Mmax is the maximum magnitude, M_o^{max} is the seismic moment for Mmax, *A=LxW* is the area of a *W*-wide and *L*-long fault, μ=3.3x10^{10} N/m^2 is the shear modulus for crustal faults (e.g., Stein and Wysession, 2003), *d* is one of the two magnitude-scaling coefficients in the relationship of Kanamori (1977) and Hanks and Kanamori (1979), *b* is the *b*-value and $\beta=b*ln(10)$. The slip rate of the fault sources is described by a uniform probability distribution within its range (i.e., 0.1 and 3.0 mm/yr for CKCF, and 0.1 and 1.5 mm/yr for TFF). Therefore, also, the activity rate of the two fault sources from equation (3B) is described by a uniform *pdf* that is parametrized into four values, each associated with a weight of 0.25 and *b* = 0.826 for CKCF and *b* = 0.959 for TFF (Table B.2).

OTHER PARAMETERS OF THE SOURCE MODEL

The depth distribution of the earthquakes in the Tien Shan and in the South Kazakh Platform is characterized by a distribution down to 40 km (see Subsection "Seismicity in the Northern Tien Shan"). The depth distribution of the model adopted here is combined in a logic tree in which each branch is shown in Table B.3.

In the Northern Tien Shan, the dominant focal mechanisms are reverse faulting, as explained in "Seismicity in the Northern Tien Shan". Therefore, we consider reverse focal mechanism for the earthquakes simulated in the source zones. The strike of the finite-fault rupture simulated for the synthetic earthquakes depends on the strike of the faults in Figure 1. The fault source TFF is a right-lateral strike-slip fault.

We assume that the minimum magnitude (i.e., the smallest earthquake considered to be of engineering significance) is Mw 4.5.

Appendix C

EARTHQUAKE SCENARIOS FOR THE SPECTRAL ACCELERATIONS

We show the distribution of 0.2 s SA (Figure C.1) and 1.0 s SA (Figure C.2) for the 1887 Verny, 1889 Chilik, and 1911 Chon-Kemin earthquakes. Short and longer period spectral accelerations relate the ground shaking to building response, albeit in a simple way. Longer period accelerations, which may be generated by a large earthquake, attenuate more slowly. They are likely to be more significant for taller buildings and, therefore, may be very important to assess the seismic hazard in Almaty (see Introduction).

DISAGGREGATION PLOTS FOR THE SPECTRAL ACCELERATIONS

The disaggregation plots for 0.2 s (i.e., short period acceleration), for 1.0 s (i.e., long period acceleration) are shown in Figures C.3-C.4. The disaggregation plot in Figure C.3a corresponds to return periods of 132 ± 75 yr and shows that the hazard is dominated by earthquakes of Mw 5.2 to 5.6 at distances of less than 10 km. As the return period increases, the dominant contribution is from earthquakes of Mw 7.0 to 7.2 (Figure C.3b). For long-period acceleration and return periods of 167 ± 108 yr, the major contribution to the hazard comes from earthquakes of Mw 7.0 to 7.6 at 20 ≤ Rjb < 30 km (Figure C.4a). For return periods of 500 ± 409 yr and 1.0 s acceleration, the hazard has a strong contribution from earthquakes of Mw 7.4 to 7.6 at 10 ≤ Rjb < 20 km (Figure C.4b). For long-period acceleration, the contribution to the hazard of Almaty from far distance sources increases, but it is still smaller than that from NISK.

The disaggregation analysis for the MSK-64 intensity shows that earthquakes of Mw 7.0 to 7.2 at distances between 10 and 20 km influence the hazard (Figure C.5).

References

Abdrakhmatov, K., S.A. Aldazhanov, B.H. Hager, M.W. Hamburger, T.A. Herring, P. Molnar, S.V. Panasyuk, M.T. Prilepin, R. Reilinger, I.S. Sadybakasov, B.J. Souter, Y.A. Tapeznikov, V.Y. Tsurkov, and A.V. Zubovich (1996). Relatively recent construction of the Tien Shan inferred from GPS measurements of present-day crustal deformation rates. *Nature* **384** 450-453.

Abdrakhmatov, K., K. Djanuzakov, and D. Delvaux (2002). Active tectonics and seismic hazard of the Issyk-Kul basin in the Kyrgyz Tian Shan, in *Lake Issyk-Kul: Its natural environment*. Klerkx, J., and B. Imanackunov (Editors), Kluwer Academic Publishers, Dordrecht, 147-160.

Abdrakhmatov, K., R. Walker, G. Campbell, A. Carr, A. Elliott, C. Hillmann, J. Hollingsworth, A. Landgraf, D. Mackenzie, A. Mukambayev, M. Rizza, and R.R. Sloan (2016). Multi-segment rupture in the July 11th 1889 Chilik earthquake (Mw 8.0-8.3), Kazakh Tien Shan, identified from remote-sensing, field survey, and paleoseismic trenching. *J. Geophys. Res.* **121** 4615-4640.

Abrahamson, N.A. (2006). Seismic hazard assessment: Problems with current practice and future developments, in *Proceedings of the First European Conference on Earthquake Engineering and Seismology*, Geneva, Switzerland, 3-8 September 2006, Keynote Address K2.

Akkar, S. and J. J. Bommer (2010). Empirical equations for the prediction of PGA, PGV and spectral accelerations in Europe, the Mediterranean Region and the Middle East, *Seismol. Res. Lett.* **81** 195-206.

Akkar, S., M.A. Sandikkaya and J.J. Bommer (2014). Empirical ground motion models for point- and extended-source crustal earthquake scenarios in Europe and the Middle East, *Bull. Earthquake Eng.* **12** 359-387.

Alinaghi, A., and F. Krüger (2014). Seismic array analysis and redetermination of depths of earthquakes in Tien-Shan: implications for strengths of the crust and lithosphere, *Geophys. J. Int.* **198** 1111-1129.

Allen, T.I., D.J. Wald, and C.B. Worden (2012). Intensity attenuation for active crustal regions, *J. Seismol.* **16** 409-433.

Amante, C. and B. Eakins (2009). ETOPO1 1Arc-Minute Global Relief Model: Procedures, data resources and analysis, *TNOAA Technical Memorandum NESDIS NGDC-24*, 19 pp.

Arrowsmith, J., C. Crosby, A. Korjenkov, E. Mamyrov, I. Povolotskaya, B. Guralnik, and A. Landgraf (2016). Surface rupture of the 1911 Kemin (Chon-Kemin) earthquake, Northern Tien Shan, Kyrgyzstan, in *Seismicity, Fault rupture and earthquake hazards in slowly deforming region*. Landgraf, A., S. Kuebler, E. Hintersberger, and S. Stein (Editors), Geol. Soc. Spec. Publ. ***432*** DOI:10.1144/SP432.10.

Bindi, D., S. Parolai, A. Oth, K. Abdrakhmatov, A. Muraliev, and J. Zchau (2011). Intensity prediction equations for Central Asia, *Geophys. J. Int.* **187** 327-337.

Bindi, D., S. Parolai, A. Gmez-Capera, M. Locati, Z. Kalmetyeva, and N. Mikhailova (2014). Locations and magnitudes of earthquakes in Central Asia from seismic intensity data, *Journal of Seismology* **18** 1-21.

Bogdanovich, K., I. Kark, B. Korol'Kov, and D. Mushketov (1914). Earthquake in Northern district of Tien-Shan, 22 December 1910 (4 January 1911), *Commission of the Geology Committee,* St. Petersburg, Russia.

Bolt, B.A., and N.A. Abrahamson (2003). Estimation of strong seismic ground motions, in *International Handbook of Earthquake and Engineering Seismology.* Lee, W.H.K., H. Kanamori, P.C. Jennings, and C. Kisslinger (Editors), Academic Press, San Diego, 983-1001.

Bommer, J.J., J. Douglas, F. Scherbaum, F. Cotton, H. Bungum, and D. Fäh (2010). On the selection of ground-motion prediction equations for seismic hazard analysis, *Seismol. Res. Lett.* **81** 783-793.

Boore, D. M., and G. M. Atkinson (2008). Ground-motion prediction equations for the average horizontal component of PGA, PGV, and 5%-damped PSA at spectral periods between 0.01s and 10.0s, *Earthquake Spectra* **24** 99-138.

Boore, D., J. Stewart, E. Seyhan, and G. Atkinson (2014). NGA-West2 equations for predicting PGA, PGV, and 5% damped PSA for shallow crustal earthquakes, *Earthquake Spectra* **30** 1057-1085.

Bormann, P., S. Wendt, and D. Di Giacomo (2013). Seismic sources and source parameters, in IASPEI: *New Manual of Seismological Observatory Practice*. Bormann, P. (Editor), GeoForschungsZentrum, Potsdam,, 3, 36-177

Bozorgnia, Y., N.A. Abrahamson, L. Al Atik, T.D. Ancheta, G.M. Atkinson, J.W. Baker, A. Baltay, D.M. Boore, K.W. Campbell, B. Chiou, R. Darragh, S. Day, J. Donahue, J., R.W. Graves, N. Gregor,

T. Hanks, I.M. Idriss, R. Kamai, T. Kishida, A. Kottke, S.A. Mahin, S. Rezaeian, B. Rowshandel, E. Seyhan, S. Shai, T. Shantz, W. Silva, P. Spudich, J.P. Stewart, J. Watson-Lamprey, K. Wooddell, and R. Youngs (2014). NGA-West2 research project, Earthquake Spectra 30, 973–987.

Burtman, V.S., S.F. Skobelev, and P. Molnar (1996). Late Cenozoic slip on the Talas-Ferghana fault, the Tien Shan, Central Asia, *Bull. Seismol. Soc. Am.* **108** 1004-1021.

Campbell, G., R. Walker, K. Abdrakhmatov, J.-L. Schwenninger, J. Jackson, J. Elliott, and A. Copley (2013). The Dzhungarian fault: Late Quaternary tectonics and slip rate of a major right-lateral strike-slip faulting the northern Tien Shan region, *J. Geophys. Res.***118** 5681-5698.

Campbell, K.W., and Y. Bozorgnia (2008). NGA ground motion model for the geometric mean horizontal component of PGA, PGV, PGD and 5% damped linear elastic response spectra for periods ranging from 0.01 to 10 s, *Earthquake Spectra* **24** 139-172.

Castellaro, S., F. Mulargia, and Y.Y. Kagan (2006). Regression problems for magnitudes, *Geophys. J. Int.*, **165** 913-930.

Chiou, B., and R.R. Youngs (2008). An NGA model for the average horizontal component of peak ground motion and response spectra, *Earthquake Spectra* **24** 173-216.

Chiou, B., and R.R. Youngs (2014). Update of the Chiou and Youngs NGA model for the average horizontal component of peak ground motion and response spectra, *Earthquake Spectra* **30** 1117-1153.

Delvaux, D., K. Abdrakhmatov, and A. Strom (2001). Landslide and surface breaks of the 1911 M 8.2 Kemin earthquake, *Landslides* **42** 1583-1592.

De Mets, C., R.G. Gordon, D.F. Argus, and S. Stein (1990). Current plate motions, *Geophys. J. Int.* **101** 425-478.

England, P., and J. Jackson (2011). Uncharted seismic risk, *Nature Geoscience* **4** 348-349.

Frankel, A.D., M.D. Petersen, C.S. Mueller, K.M. Haller, R.L. Wheeler, E.V. Leyandecker, R.L. Wesson, S.C. Harmsen, C.H. Cramer, D.M. Perkins, K.S. Rukstales (2002). Documentation for the 2002 update of the national seismic hazard maps, *U.S. Geological Survey Open-file report 02-420*.

Giardini, D. (1999). The Global Seismic Hazard Assessment Program (GSHAP) – 1992/1999, *Ann. Geophys*. **42(6)** 957-974.

Ghose, S., R.J. Mellors, A. Korjenkov, M.W. Hamburger, T.L. Pavlis, G.L. Pavlis, M. Omuraliev, E. Mamyrov, and A. Mraliev (1997). The Ms = 7.3 1992 Suusamyr, Kyrgyzstan, earthquake in the Tien Shan: 2. Aftershock focal mechanisms and surface deformation, *Bull. Seismol. Soc. Am.* **87** 23-28.

Ghose, S., M.W. Hamburger, and C.J. Ammon (1998). Source parameters of moderate-sized earthquakes in the Tien Shan, Central Asia from regional moment tensor inversion. *Geophys. Res. Lett.* **25** 3181-3184.

Grützner, C., R.T. Walker, K. Abdrakhmatov, A. Makambayev, A. J. Elliott, and J. R. Elliott (2017). Active tectonics around Almaty and along the Zailisky Alatau Rangefront, *Tectonics.* 36 2192-2226.

Gutenberg, B., and C.F. Richter (1954). *Seismicity of the Earth and associated phenomena*, Princeton University Press, Princeton, New Jersey.

Hanks, T., and H. Kanamori (1979). A moment magnitude scale, *J. Geol. Res.* **84** 2348-2350.

Henni, P.H.O., C.J. Fyfe, and P.C. Marrow (1998). The BGS World Seismicity Database, *Technical Rept. WL/98/13, 9 pp*.

IAEA - International Atomic Energy Agency (2010). Seismic hazards in site evaluation for nuclear installations. *Specific Safety Guide No. SSG-9, IAEA, Vienna*.

Johnston, A.C., K. J. Coppersmith, L. R. Kanter, and C. A. Cornell (1994). The earthquakes of stable continental regions, *EPRI Report*, Electric Power Research Institute, Palo Alto.

Kanamori, H. (1977). The energy release in great earthquakes, *J. Geophys. Res.* **82** 2981-2987.

Karnik, V. (1962). Amplitude-distance curves of surface waves at short epicentral distances, *Stud. Geophys. Geod.* **6** 340-346.

King, S.A., V.I. Khalturin, and B.E. Tucker (1999). *Seismic hazard and building vulnerability in Post-Soviet Central Asian Republics,* Springer, Berlin.

Kondorskaya, N., and N. Shebalin (1977). *New catalogue of large earthquakes in the USSR area*, Nauka Publishing House, Moscow, Russia.

Kondorskaya, N., and N. Shebalin (1982). *New catalogue of strong earthquakes in the USSR from ancient times through 1977*, National Oceanic and Atmospheric Administration, Boulder, Colorado.

Korjenkov, A., K. Baipakov, C. Chang, Y. Peshkov, and T. Savelieva (2003). Traces of ancient earthquakes in Medieval cites along the Silk Road, northern Tien Shan and Dzhungaria, *Turk. J. Earth Sci*. **12** 241-261.

Krüger, F., A. Kulikova, and A. Landgraf (2016). Instrumental magnitude constraints for the 11 July 1889, Chilik earthquake, in *Seismicity, Fault rupture and earthquake hazards in slowly deforming region*. Landgraf, A., S. Kuebler, E. Hintersberger, and S. Stein (Editors), Geol. Soc. Spec. Publ. ***432*** DOI:10.1144/SP432.8.

Kulikova, G., and F. Krüger (2015). Source process of the 1911 M8.0 Chon-Kemin earthquake: investigation results by analogue seismic records, *Geophys. J. Int.* **201** 1891-1911.

Landgraf, A., A. Dzhumabaeva, K. Abdrakhmatov, M.R. Stecker, E.A. Macaulay, J. Arrowsmith, H. Sudhaus, F. Preusser, G. Rugel, and S. Merchel (2016a). Repeated large-magnitude earthquakes in a tectonically active, low-strain continental interior: The Northern Tien Shan, Kyrgyzstan, *J. Geophys. Res. Solid Earth Planets* **121** 3888-3910.

Landgraf, A, S. Kuebler, E. Hintersberger, and S. Stein (2016b). Active tectonics, earthquakes and paleoseismicity in slowly deforming continents, *Geol. Soc. Spec. Publ.* **432** DOI:10.1144/SP432.13.

Leonard, M. (2010). Earthquake fault scaling: Self-consistent relating of rupture length, width, average displacement, and moment release, *Bull. Seismol. Soc. Am.* **100** 1971-1988.

Liu, M., and Stein, S. (2016). Mid-continent earthquakes: Spatio-temporal occurrences, causes and hazards. *Earth-Sci. Rev.* **162** 364-386.

McGuire, R.K. (2004). *Seismic Hazard and Risk Analysis,* Earthquake Engineering Research Institute, Oakland.

Mellors, R.J., F.L. Vernon, G.L. Pavlis, G.A. Abers, M.W. Hamburger, S. Ghose, and B. Iliasov (1997). The Ms=7.3 1992 Suusamyr, Kyrgyzstan, earthquake: 1. Constraints on fault geometry and source parameters based on aftershocks and body-wave modelling, *Bull. Seismol. Soc. Am.* **87** 11-22.

Mikhailova, N., A. Mukambayev, I. Aristova, G. Kulikova, S. Ullah, M. Pilz, and D. Bindi (2015). Central Asia earthquake catalogue from ancient time to 2009, *Ann. Geophys*. **58** DOI:10.4401/ag-6681.

Molnar, P., and Q. Deng (1984). Faulting associated with large earthquakes and the average rate of deformation in central and eastern Asia, *J. Geophys. Res.* **89** 6203-6228.

Molnar, P., and S. Ghose (2000). Seismic moments of major earthquakes and rate of shortening across the Tien Shan, *Geophys. Res. Lett.* **27** 2377-2380.

Mushketov, I. (1890). The Verny earthquake 28th May (9th June) 1887. *Memoirs of the Geological Committee* **10(1)** St. Petersburg, Russia.

Mushketov, I. (1891). Materials for investigation of earthquakes in Russia. *Annex to the 27th volume of tidings of the Imperial Russian Geographical Society*.

Musson, R.M.W. (2000). The use of Monte Carlo simulations for seismic hazard assessment in the UK, *Ann. Geophys.* **43** 1-9.

Musson, R.M.W. (2012). The effect of magnitude uncertainty on activity rates, *Bull. Seismol Soc. Am.* **102** 2771-2775.

Musson, R.M.W. (2015). Bipartite earthquake magnitude-frequency distributions*, IUGG/IASPEI 38th General Assembly*. Oral Presentation, Prague, Czech Republic, 22 June-2 July 2015.

Musson, R.M.W., and S. Sargeant (2007). Eurocode 8 seismic hazard zoning maps for the UK. *BGS Report CR/07/125,* 62 pp.

ODI – Overseas Development Institute (2016). Earthquake science and hazard in Central Asia. *Conference Summary Report,* 32 pp.

Pagani, M., D. Monelli, G. Weatherill, L. Danciu, H. Crowley, V. Silva, P. Henshaw, M. Nastasi, L. M. S. Panzeri, and D. Viganó (2014). OpenQuake engine: An open hazard (and risk) software for Global Earthquake Model*, Seismol. Res. Lett.* **85** 692-702.

Paramzin, A.M. (2005). Qualitative characteristic of the selected building objects in Almaty Oblast and Almaty City (in Russian), in *Risk Management on the Local Level in Earthquake Prone Zones of Kazakhstan,* United Nations Development Programme, Almaty, 76-86 (in Russian).

Parolai, S., J. Zschau, and U. Begaliev (2015). Earthquake Model Central Asia: seismic hazard and risk assessment in Central Asia, *Ann. Geophys*. **58**.

Pilz, M., T. Abakanov, K. Abdrakhmatov, D. Bindi, T. Boxberger, B. Moldobekov, S. Orunbaev, N. Sylacheva, S. Ullah, S. Usupaev, P. Yasunov, and S. Parolai (2015). An overview on the seismic microzonation and site effect studies in Central Asia, *Ann. Geophys*. **58** DOI: 10.4401/ag-6662.

Reasenberg, P.A. (1985). Second-order moment of Central California seismicity, 1969-1982, *J. Geophys. Res.* **90** 5479-5495.

Reiter, L. (1990). *Earthquake Hazard Analysis: Issues and Insights,* Columbia University Press, New York.

Rhoades, D.A. and D.J. Dowrick (2000). Effects of magnitude uncertainties on seismic hazard estimates, *Proc.12th World Conf. Earthquake Eng*., Wellington, New Zealand, Paper 1179.

Scordilis, E.M. (2006). Empirical global relations converting Ms and mb to moment magnitude, *Journal of Seismology* **10** 225-236.

Silacheva, N.V., U.K. Kulbayeva, and N.A. Kravchenko (2017). Probabilistic seismic hazard assessment of Kazakhstan and Almaty city in peak ground accelerations. *Geodesy Geodynamics.* DOI:10.1016/j.geog.2017.11.002.

Sloan, R.A., J. Jackson, D. McKenzie, and K. Priestley (2011). Earthquake depth distribution in Central Asia, and their relations with lithosphere thickness, shortening, and extension, *Geophys. J. Int.* **185** 1-29.

Stepp, J.C. (1972). Analysis of completeness of the earthquake sample in the Puget Sound Area and its effect on statistical estimates of earthquake hazard, *First International Conference on Microzonation*, Seattle, **2** 897-909.

Stein, S., and M. Wysession (2003). *An Introduction to Seismology, Earthquakes, and Earth Structure,* Wiley-Blackwell Publishing, Oxford.

Stein, S., R.J. Geller, and M. Liu (2012). Why earthquake hazard maps often fail and what to do about it?. *Tectonophysics.* **562/553** 1-25.

Tapponnier, P., and P. Molnar (1979). Active faulting and Cenozoic tectonics of the Tien Shan, Mongolia and Baykal regions, *J. Geophys. Res.* **84** 3425-3456.

Tatevossian, R.E. (2007). The Verny, 1887, earthquake in Central Asia: Application of the INQUA scale, based on coseismic environmental effects, *Quatern. Int.* **173** 23-29.

Thompson, S.C., R.J. Weldon, C.M. Rubin, and K. Abdrakhmatov (2002). Late Quaternary slip rates across the central Tien Shan, Kyrgyzstan, Central Asia, *J. Geophys. Res.* **107** 10.1029/2001JB000596.

Tibaldi, A., E. Graziotto, F. Forcella, and V. Gapich (1997). Morphotectonic indicators of Holocene faulting in central Tien Shan, Kazakhstan, and geodynamic implications, *J. Geodyn*. **23** 23-45.

Ullah, S., D. Bindi, M. Pilz, L. Danciu, G. Weatherill, E. Zuccolo, A. Ischuk, N. Mikhailova, K. Abdrakhmatov, and S. Parolai (2015). Probabilistic seismic hazard assessment for Central Asia, *Ann. Geophys*. **58** DOI:10.4401/ag-6687.

Ulomov, V.I., and the GSHAP Region 7 Working Group (1999). Seismic hazard of Northern Eurasia, *Ann. Geophys*. **42(6)** 1023-1038.

Youngs, R.R., and K.J. Coppersmith (1985). Implications of fault slip rates and earthquake recurrence models to probabilistic seismic hazard estimates. *Bull. Seismol. Soc. Am.***75 (4)** 939-964.

Wong, I., W. Silva, S. Olig, P. Thomas, D. Wright, F. Ashland, N. Gregor, J. Pechmann, M. Dober, G. Christenson, and R. Gerthl (2002). Earthquake Scenario and Probabilistic Ground Shaking Maps for the Salt Lake City, Utah, Metropolitan Area. *Utah Geological Survey Miscellaneous Publication MP02-05,* 55pp.

Wessel, P., W. Smith, R. Scharroo, J. Luis, and F. Wobbe (2013). Generic Mapping Tools: Improved version released, *EOS, Trans. AGU.* **94** 409-410.

Zhao, J.X., J. Zhang, A. Asano, Y. Ohno, T. Oouchi, T. Takahashi, H. Ogawa, K. Irikura, H.K. Thio, P.G. Somerville, Y. Fukushima, and Y. Fukushima (2006). Attenuation relations of strong ground motion in Japan using site classification based on predominant period. *Bull. Seismol. Soc. Am***.** **96(3)** 898–913.

Zöller, G., S. Ullah, D. Bindi, S. Parolai, and N.N. Mikhailova (2017). The largest expected earthquake magnitudes in Central Asia: statistical inference from an earthquake catalogue with uncertain magnitudes. , in *Seismicity, Fault rupture and earthquake hazards in slowly deforming region*. Landgraf, A., S. Kuebler, E. Hintersberger, and S. Stein (Editors), Geol. Soc. Spec. Publ. ***432*** 29-32.

Zubovich, A., X. Wang, Y. Scherba, G. Schelochkov, R. Reilinger, C. Reigber, O. Mosienko, P. Molnar, W. Michajilow, W. Makarov, J. Li, S. Kuzikov, T. Herring, M. Hamberger, B. Hager, Y. Dang, V. Bragin, and R. Beisenbaev (2010). GPS velocity field for the Tien Shan and surrounding regions, *Tectonics* **29** doi:10.1029/2010TC002772.

List of figure captions

Figure 1: (a) Topographic map of Asia from the global model ETOPO1 (Amante and Eakins, 2009). The white lines represent the plate boundaries and the dashed rectangle indicates the study area. (b) Seismotectonic map of the Northern Tien Shan mountain belt where historical seismicity (before 1964) is indicated by squares and instrumental seismicity (after 1964), by circles. Symbol size is proportional to magnitude. Events of unknown depth are white. Tectonic structures are from 1) the Kyrgyz Institute of Seismology and digitized by the Active Tectonics Group at Arizona State University; 2) Hager and co-workers at Central Washington University, and Bogdanovich et al. (1914) and digitized by the Active Tectonics Group at Arizona State University. CKCF and TFF stand for Chon-Kemin-Chilik fault and Talas-Ferghana fault, respectively. The Ferghana Basin, Lake Issyk-Kul, and Ili basin are indicated by FB, LIK, and ILI, respectively.

Figure 2: Epicentral location (solid circles) and fault ruptures (solid lines) of the three scenario earthquakes considered in this study. The dashed lines indicate the fault segments mapped by Abdrakhmatov et al. (2016) that potentially ruptured during the 1889 Chilik earthquake. The irregular lines indicate the surface rupture mapped by Arrowsmith et al. (2016) for the 1911 Chon-Kemin earthquake. See Figure 1 for details on the tectonic structures.

Figure 3: Isoseismals for the 1889 Chilik (Mushketov, 1891) and 1911 Chon-Kemin (Bogdanovich et al., 1914) earthquakes are indicated in grey and black, respectively. See Figure 2 for details on epicenters (solid circles) and fault ruptures (solid and dashed lines) of the two earthquakes.

Figure 4: Distribution of PGA, together with its standard deviation, for (a) the 1887 Verny earthquake; (b) the 1889 Chilik earthquake; and (c) the 1911 Chon-Kemin earthquake. The mean ground motions and their standard deviations have been computed from 1000 scenarios. The white star indicates the city of Almaty. The white dot and the white line describe the epicenter and the fault rupture, respectively.

Figure 5: Distribution of MSK-64 intensity for (a) the 1887 Verny earthquake; (b) the 1889 Chilik earthquake; and (c) the 1911 Chon-Kemin earthquake. The white star indicates the city of Almaty. The white dot and the white line describe the epicenter and the fault rupture, respectively.

Figure 6: Seismic source model used in this study. The star denotes the site used for PSHA.

Figure 7: Magnitude-frequency recurrence for the source zone NISK. The solid line indicates the seismicity of the normal population of earthquakes predicted by the Gutenberg-Richter law in the range Mw 4.5 to 6.9; and the dashed line describes the seismicity of the additional

population of earthquakes predicted by the Gutenberg-Richter law in the range Mw 7.0 to 8.5. The grey area describes the region outside the completeness threshold of the earthquake catalogue for Mw ≥ 4.5.

Figure 8: Seismic hazard curves for the site in Almaty. The solid lines are for the source model that consists of 16 zones and two faults; and the dashed lines are for the source model that consists of 16 zones only. The estimated ground motion values, together with their error-bars, for the scenario earthquakes are indicated by the circles.

Figure 9: Disaggregation by magnitude Mw, Joyner-Boore distance and epsilon ε for two pairs of PGA values and return periods: (a) 0.23 ± 0.08 g and 139 ± 81 yr; and (b) 0.49 ± 0.19 g and 588 ± 514 yr.

Figure B.1: Magnitude-frequency recurrence for the study area. The grey area describes the region outside the completeness threshold of the earthquake catalogue for Mw ≥ 4.5.

Figure B.2: Activity rates and b-values for the individual zones in the source model. (a) The earthquake catalogue within the completeness thresholds set out in Table A.2 and the source zone model. (b) The activity rate and (d) the *b*-value of each source zone, together with (c, e) the standard deviation (maps on the right). The white star denotes the site.

Figure C.1: Distribution of 0.2 s SA, together with its standard deviation, for (a) the 1887 Verny earthquake; (b) the 1889 Chilik earthquake; and (c) the 1911 Chon-Kemin earthquake. The mean ground motions and their standard deviations have been computed from 1000 scenarios. The white star indicates the city of Almaty. The white dot and the white line describe the epicenter and the fault rupture, respectively.

Figure C.2: Distribution of 1.0 s SA, together with its standard deviation, for (a) the 1887 Verny earthquake; (b) the 1889 Chilik earthquake; and (c) the 1911 Chon-Kemin earthquake. The mean ground motions and their standard deviations have been computed from 1000 scenarios. The white star indicates the city of Almaty. The white dot and the white line describe the epicenter and the fault rupture, respectively.

Figure C.3: Disaggregation by magnitude Mw, Joyner-Boore distance and epsilon ε for two pairs of 0.2 s SA values and return periods: (a) 0.48 ± 0.17 g and 132 ± 75 yr; and (b) 1.11 ± 0.44 g and 588 ± 509 yr.

Figure C.4: Disaggregation by magnitude Mw, Joyner-Boore distance and epsilon ε for two pairs of 1.0 s SA values and return periods: (a) 0.17 ± 0.07 g and 167 ± 108 yr; and (b) 0.32 ± 0.14 g and 500 ± 409 yr.

Figure C.5: Disaggregation by magnitude Mw, Joyner-Boore distance and epsilon ε for MSK-64 intensity VIII ± I and the return period of 161 ± 483 yr.

Table 1: Rupture model of the scenario earthquakes.

Parameter	**1887 Verny**	**1889 Chilik**	**1911 Chon-Kemin**
Epicenter	43.10°N$^{\#}$, 76.80°E$^{\#}$	43.17 ± 0.50§ °N, 78.55 ± 0.50§ °E	42.80 ± 0.28† °N, 77.30 ± 0.49† °E
Mw	7.3 ± 0.2‡	8.2 ± 0.2‡	8.0 ± 0.1†
Dip [°]	60$^{\#}$	70$^{\#}$	52 ± 10†
Rake [°]	98$^{\#}$	60$^{\#}$	98 ± 10†
Hypocentral depth [km]	20$^{\#}$	40$^{\#}$	20 ± 3†
Rupture length [km]	75 ± 20*	260 ± 71*	202 ± 28*
Down-dip width [km]	31 ± 8*	42$^{\#}$	50 ± 5*
Geometry of the fault trace**: latitude [°]; longitude [°]	43.09; 76.39 43.13; 76.58 43.15; 76.96 43.29; 77.21 43.31; 77.35	42.83; 76.78 43.00; 77.61 43.01; 78.25 43.80; 79.50	42.71; 75.85 42.82; 76.83 42.82; 78.34

*The standard deviation is estimated from the error propagation.

$^{\#}$ The value is hypothetical.

† The standard deviation is from Kulikova and Krüger (2015).

‡ The standard deviation is from Scordilis (2006).

§ The standard deviation is reported in Bindi et al. (2014).

** Simplified geometry of the ruptured fault trace based on published data and used in the DSHA.

Table 2: Distance metrics for the scenario earthquakes.

Distance	**1887 Verny**	**1889 Chilik**	**1911 Chon-Kemin**
Source-site distance [km]	21.4	134.4	62.5
Rjb [km]	0.0	32.9	20.6

Table 3: Mean values for PGA, 0.2 s and 1.0 s SA, and MSK-64 intensity in Almaty for the scenario earthquakes using v_{s30}=760 m/s.

Ground motion parameter	**1887 Verny**	**1889 Chilik**	**1911 Chon-Kemin**
PGA [g]	0.49 ± 0.19	0.167 ± 0.06	0.23 ± 0.08
0.2 s SA [g]	1.11 ± 0.44	0.34 ± 0.12	0.48 ± 0.17
1.0 s SA [g]	0.32 ± 0.14	0.14 ± 0.06	0.17 ± 0.07
MSK-64	VIII ± I	VIII ± I	VIII ± I

Table 4: Sensitivity analysis of the ground shaking scenario for the 1911 Chon-Kemin earthquake*.

Number	**Test**	**Parameter**	**PGA ± σ [g]**	**0.2 s SA ± σ [g]**	**1.0 s SA ± σ [g]**
1	Site conditions	Soft rock (360 < Vs30 < 760 m/s)	0.27 ± 0.09	0.59 ± 0.20	0.25 ± 0.10
2	GMPE	Boore et al. (2014)	0.23 ± 0.07	0.47 ± 0.15	0.17 ± 0.06
3	GMPE	Chiou and Youngs (2014)	0.23 ± 0.07	0.52 ±0.17	0.15 ± 0.05
4	GMPE	Akkar et al. (2014)	0.23 ± 0.09	0.45 ± 0.18	0.19 ± 0.08
5	Focal mechanism	Dip = 45°	0.32 ± 0.11	0.69 ± 0.25	0.23 ± 0.10
6	Focal mechanism	Rake = 60° , dip = 65°	0.15 ± 0.05	0.30 ± 0.11	0.12 ±0.06
7	Multi-segmented rupture	Varying dips	0.19 ± 0.06	0.39 ± 0.14	0.14 ± 0.06

*The second column indicates the parameter changed in each test; and the third, fourth and fifth columns show the estimate of ground motion parameter for the site in Almaty.

Table 5: Values of maximum magnitude (Mmax) and weights (WGTs) of the source model.

Tectonic unit	**Source**	**Mmax1**	**WGT1**	**Mmax2**	**WGT2**	**Mmax3**	**WGT3**	**Mmax4**	**WGT4**
Western Tien Shan	ALAI	7.5	0.20	8.0	0.60	8.2	0.20	-	-
	FERR	7.5	0.20	8.0	0.60	8.2	0.20	-	-
Lower Northern Tien Shan	ATBA	7.0	0.25	7.5	0.25	8.0	0.25	8.2	0.25
	KERS	7.0	0.25	7.5	0.25	8.0	0.25	8.2	0.25
	NARY	7.0	0.25	7.5	0.25	8.0	0.25	8.2	0.25
	SISK	7.0	0.25	7.5	0.25	8.0	0.25	8.2	0.25
Eastern Tien Shan	CTS1	8.2	0.40	8.3	0.40	8.5	0.20	-	-
	CTS2	8.2	0.40	8.3	0.40	8.5	0.20	-	-
	ILI	8.2	0.40	8.3	0.40	8.5	0.20	-	-
Foreland Tien Shan	FTS1	8.2	0.40	8.3	0.40	8.5	0.20	-	-
	FTS2	8.2	0.40	8.3	0.40	8.5	0.20	-	-
	FTS3	8.2	0.40	8.3	0.40	8.5	0.20	-	-
Kazakh Plat.	KZPL	6.5	0.25	7.0	0.25	7.5	0.25	8.0	0.25
Upper Northern Tien Shan	KYRG	8.2	0.40	8.3	0.40	8.5	0.20	-	-
	NISK	8.2	0.40	8.3	0.40	8.5	0.20	-	-
	SUUS	8.2	0.40	8.3	0.40	8.5	0.20	-	-
Fault sources	CKCF	8.2	0.40	8.3	0.40	8.5	0.20	-	-
	TFF	8.2	0.40	8.3	0.40	8.5	0.20	-	-

Table 6: Return periods of the ground motion values for a site in Almaty for the scenario earthquakes.

Ground motion parameter	**1887 Verny**	**1889 Chilik**	**1911 Chon-Kemin**
PGA [g]	588 ± 514	81 ± 44	139 ± 81
0.2 s SA [g]	588 ± 509	76 ± 41	132 ± 75
1.0 s SA [g]	500 ± 409	120 ± 80	167 ± 108
MSK-64	161 ± 483	161 ± 483	161 ± 483

Table 7: Comparison of the hazard results for 475 –year return period between this study and previous works.

Study	**MSK-64**	**PGA**
Ulomov et al. (1999)	IX	-
Ullah et al. (2015)	VII-VIII	-
Silacheva et al. (2017)	-	0.36-0.44
This study	VIII-IX	0.44

Table A.1: Hierarchy of magnitude selected among the available magnitude estimates in the ISC database.

Number	Magnitude	Agency
1	Mw	Global Centroid Moment Tensor
2	Mw	National Earthquake Information Centre
3	Ms	International Seismological Centre
4	mb	International Seismological Centre
5	Ms	National Earthquake Information Centre
6	mb	National Earthquake Information Centre
7	Ms	International Data Centre for Comprehensive Nuclear-Test-Ban Treaty Organization
8	mb	International Data Centre for Comprehensive Nuclear-Test-Ban Treaty Organization
9	Ms	European-Mediterranean Seismological Centre
10	mb	European-Mediterranean Seismological Centre
11	Ms/mb	Agency providing the hypocentral location

Table A.2: Completeness periods for the catalogue.

Mw	Completeness period
4.5	1970
5.0	1965
5.5	1925
6.0	1875
6.5	1875
7.0	1875
7.5	1875
8.0	1875

Table B.1: Number of earthquakes used for the recurrence statistics, activity rate N (≥ Mw 4.5) and *b*-value of the source model.

Tectonic unit	**Source**	**Number of earthquakes**	**N(≥ Mw 4.5)**	**b-value**
Western Tien Shan	ALAI	59	1.15 ± 0.15	1.004 ± 0.083
	FERR	28	0.56 ± 0.10	1.03 ± 0.10
Lower Northern Tien Shan	ATBA	38	0.75 ± 0.12	1.009 ± 0.095
	KERS	23	0.468 ± 0.095	1.11 ± 0.11
	NARY	28	0.56 ± 0.10	1.030 ± 0.10
	SISK	21	0.415 ± 0.088	1.00 ±0.11
Eastern Tien Shan	CTS1	49	0.97 ± 0.14	1.037 ± 0.090
	CTS2	53	1.04 ± 0.14	1.009 ± 0.086
	ILI	14	0.269 ± 0.070	0.91 ± 0.11
Foreland Tien Shan	FTS1	38	0.72 ± 0.11	0.894 ± 0.089
	FTS2	248	4.84 ± 0.30	0.994 ± 0.047
	FTS3	14	0.273 ± 0.071	0.95 ± 0.11
Kazakh Plat.	KZPL	11	0.209 ± 0.061	0.86 ± 0.11
Upper Northern Tien Shan	KYRG	22	0.426 ± 0.089	0.95 ± 0.10
	NISK	49	0.90 ± 0.13	0.826 ± 0.078
	SUUS	28	0.55 ± 0.10	0.97 ± 0.10

Table B.2: Values of slip rates and activity rates of the fault sources CKCF and TFF.

CKCF				TFF			
Slip rate [mm/yr]	Activity rate (≥ Mw4.5)	b-value	Weight	Slip rate [mm/yr]	Activity rate (≥ Mw4.5)	b-value	Weight
0.1	-2.0192	0.826	0.25	0.1	-1.7579	0.959	0.25
1.0	-1.0192	0.826	0.25	0.5	-1.0590	0.959	0.25
2.0	-0.7181	0.826	0.25	1.0	-0.7579	0.959	0.25
3.0	-0.5421	0.826	0.25	1.5	-0.5819	0.959	0.25

Table B.3: Values of hypocentral depths (h, km), in kilometers, and weights (WGTs) of the source model.

Tectonic unit	Source	h1	WGT1	h2	WGT2	h3	WGT3	h4	WGT4	h5	WGT5	h6	WGT6
Western Tien Shan	ALAI	5	0.10	10	0.20	15	0.25	20	0.25	25	0.20	-	-
	FERR	5	0.10	10	0.20	15	0.25	20	0.25	25	0.20	-	-
Lower Northern Tien Shan	ATBA	5	0.10	10	0.20	15	0.25	20	0.25	25	0.20	-	-
	KERS	5	0.10	10	0.20	15	0.25	20	0.25	25	0.20	-	-
	NARY	5	0.10	10	0.20	15	0.25	20	0.25	25	0.20	-	-
	SISK	5	0.10	10	0.20	15	0.25	20	0.25	25	0.20	-	-
Eastern Tien Shan	CTS1	10	0.30	20	0.30	30	0.20	40	0.20	-	-	-	-
	CTS2	10	0.30	20	0.30	30	0.20	40	0.20	-	-	-	-
	ILI	10	0.30	20	0.30	30	0.20	40	0.20	-	-	-	-
Foreland Tien Shan	FTS1	10	0.25	20	0.25	30	0.25	40	0.10	-	-	-	-
	FTS2	10	0.25	20	0.25	30	0.25	40	0.10	-	-	-	-
	FTS3	10	0.25	20	0.25	30	0.25	40	0.10	-	-	-	-
Kazakh Plat.	KZPL	10	0.30	20	0.30	30	0.20	40	0.20	-	-	-	-
Upper Northern Tien Shan	KYRG	5	0.10	10	0.20	15	0.25	20	0.25	25	0.20	-	-
	NISK	10	0.15	15	0.30	20	0.30	25	0.15	30	0.05	40	0.05
	SUUS	5	0.10	10	0.20	15	0.25	20	0.25	25	0.20	-	-
Fault Sources	CKCF	10	0.20	15	0.20	20	0.30	25	0.30	-	-	-	-
	TFF	10	0.20	15	0.20	20	0.30	25	0.30	-	-	-	-

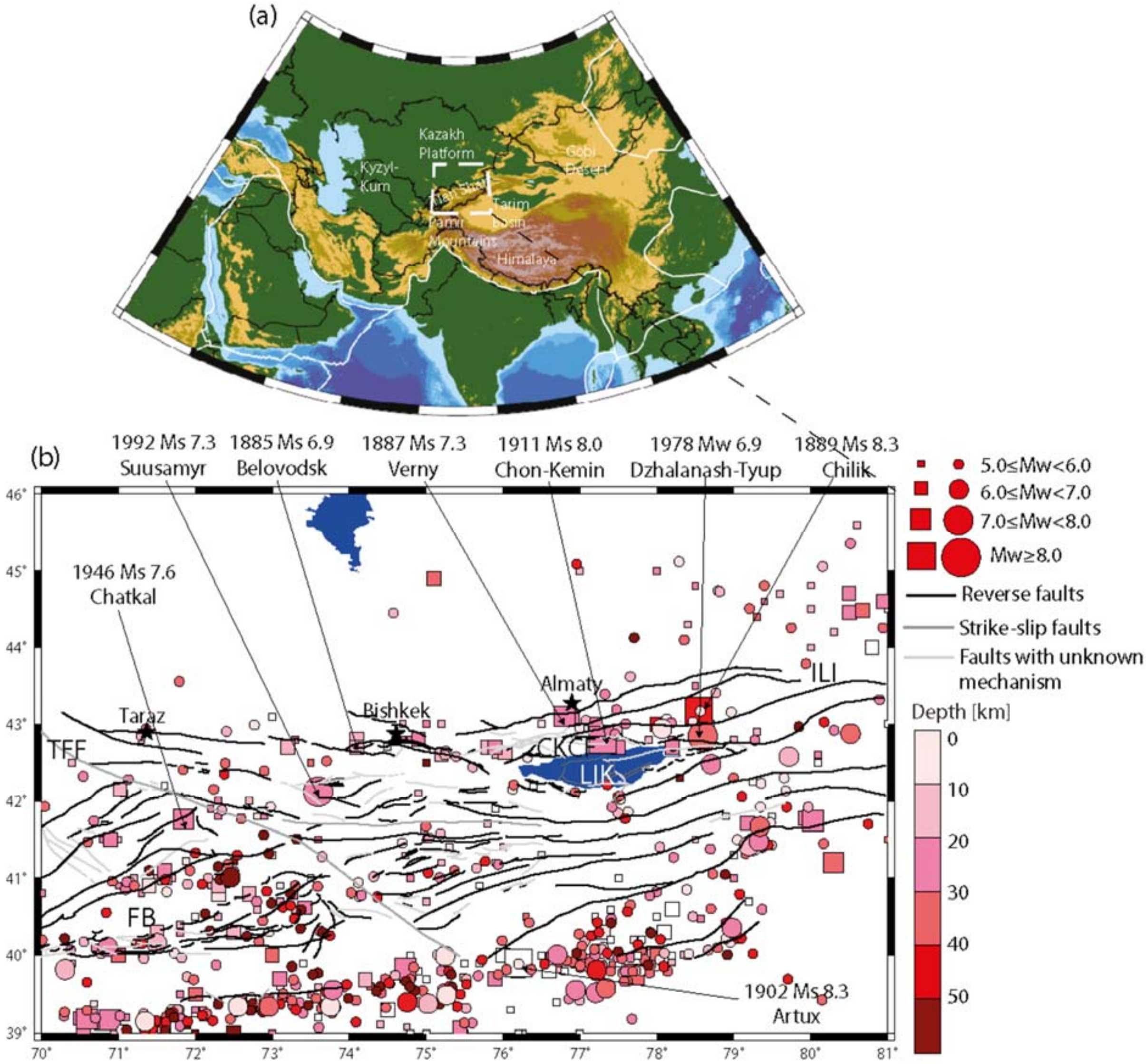

Figure 1: (a) Topographic map of Asia from the global model ETOPO1 (Amante and Eakins, 2009). The white lines represent the plate boundaries and the dashed rectangle indicates the study area. (b) Seismotectonic map of the Northern Tien Shan mountain belt where historical seismicity (before 1964) is indicated by squares and instrumental seismicity (after 1964), by circles. Symbol size is proportional to magnitude. Events of unknown depth are white. Tectonic structures are from 1) the Kyrgyz Institute of Seismology and digitized by the Active Tectonics Group at Arizona State University; 2) Hager and co-workers at Central Washington University, and Bogdanovich et al. (1914) and digitized by the Active Tectonics

Group at Arizona State University. CKCF and TFF stand for Chon-Kemin-Chilik fault and Talas-Ferghana fault, respectively. The Ferghana Basin, Lake Issyk-Kul, and Ili basin are indicated by FB, LIK, and ILI, respectively.

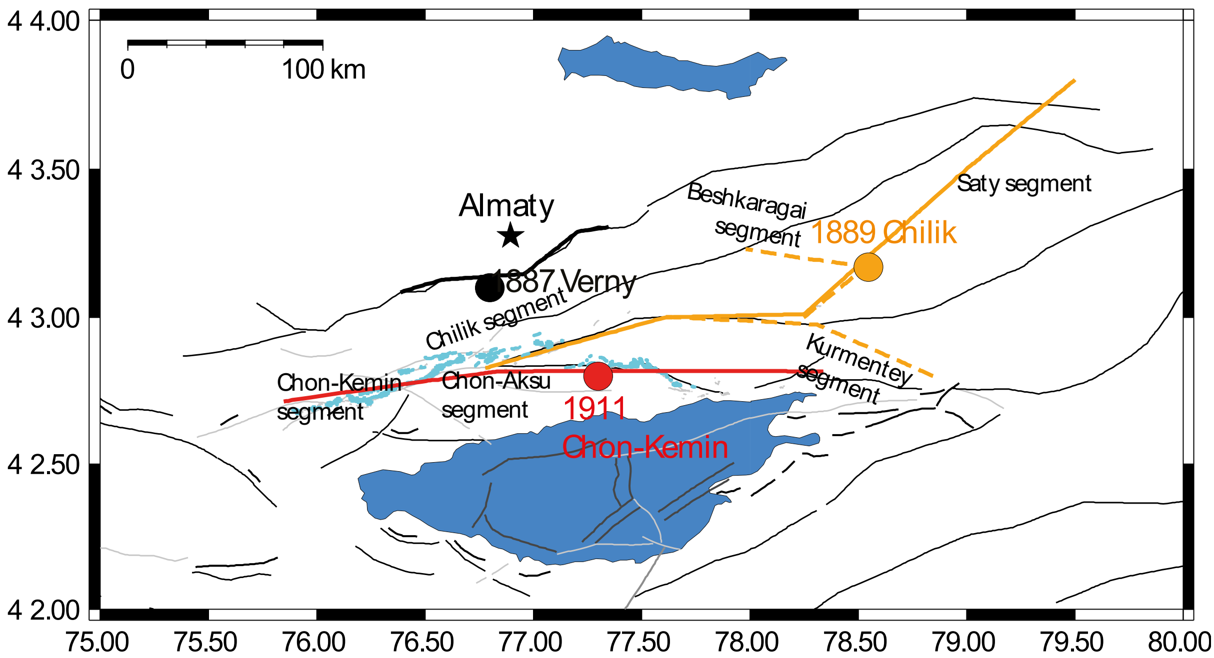

Figure 2: Epicentral location (solid circles) and fault ruptures (solid lines) of the three scenario earthquakes considered in this study. The dashed lines indicate the fault segments mapped by Abdrakhmatov et al. (2016) that potentially ruptured during the 1889 Chilik earthquake. The irregular lines indicate the surface rupture mapped by Arrowsmith et al. (2016) for the 1911 Chon-Kemin earthquake. See Figure 1 for details on the tectonic structures.

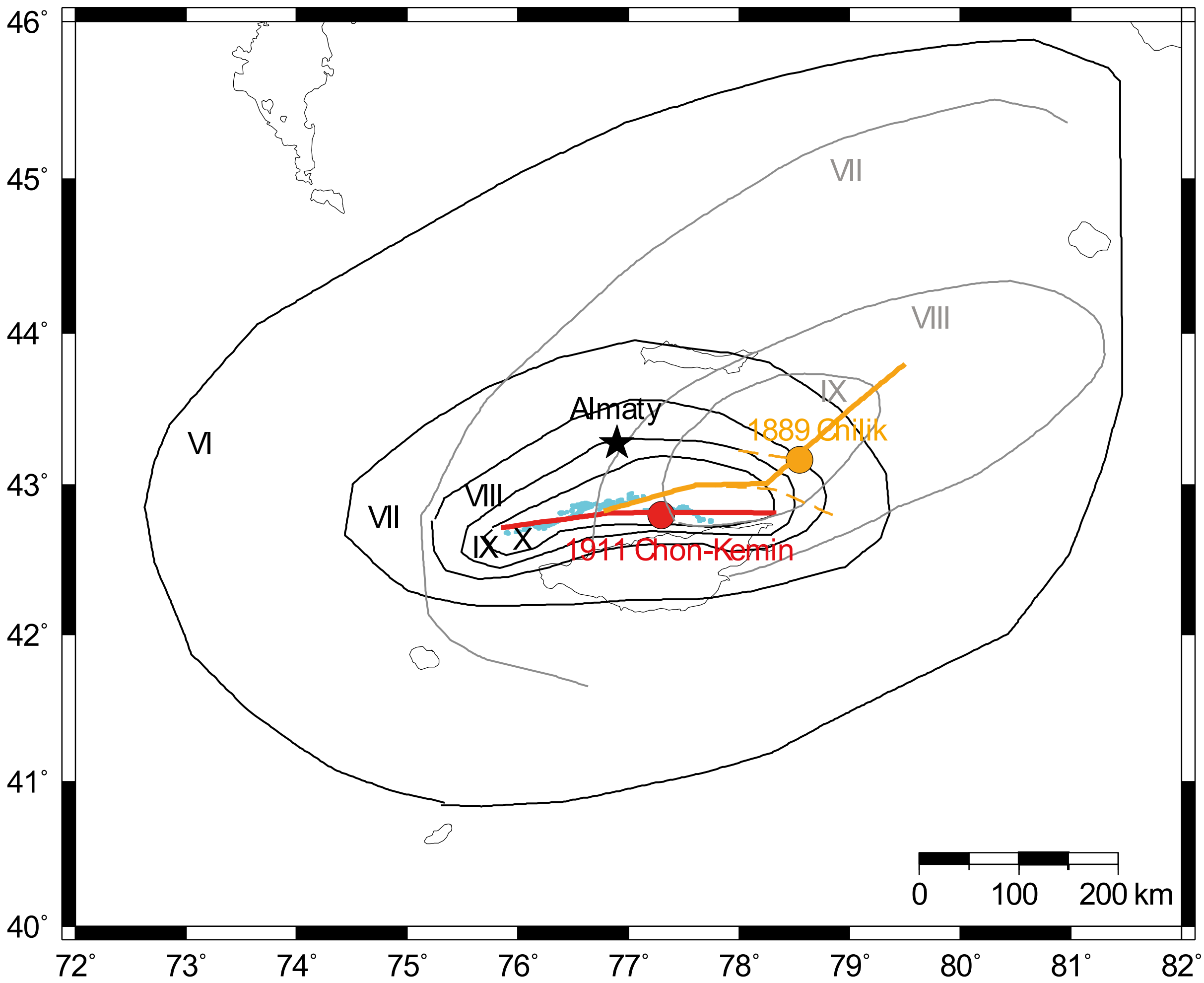

Figure 3: Isoseismals for the 1889 Chilik (Mushketov, 1891) and 1911 Chon-Kemin (Bogdanovich et al., 1914) earthquakes are indicated in grey and black, respectively. See Figure 2 for details on epicenters (solid circles) and fault ruptures (solid and dashed lines) of the two earthquakes.

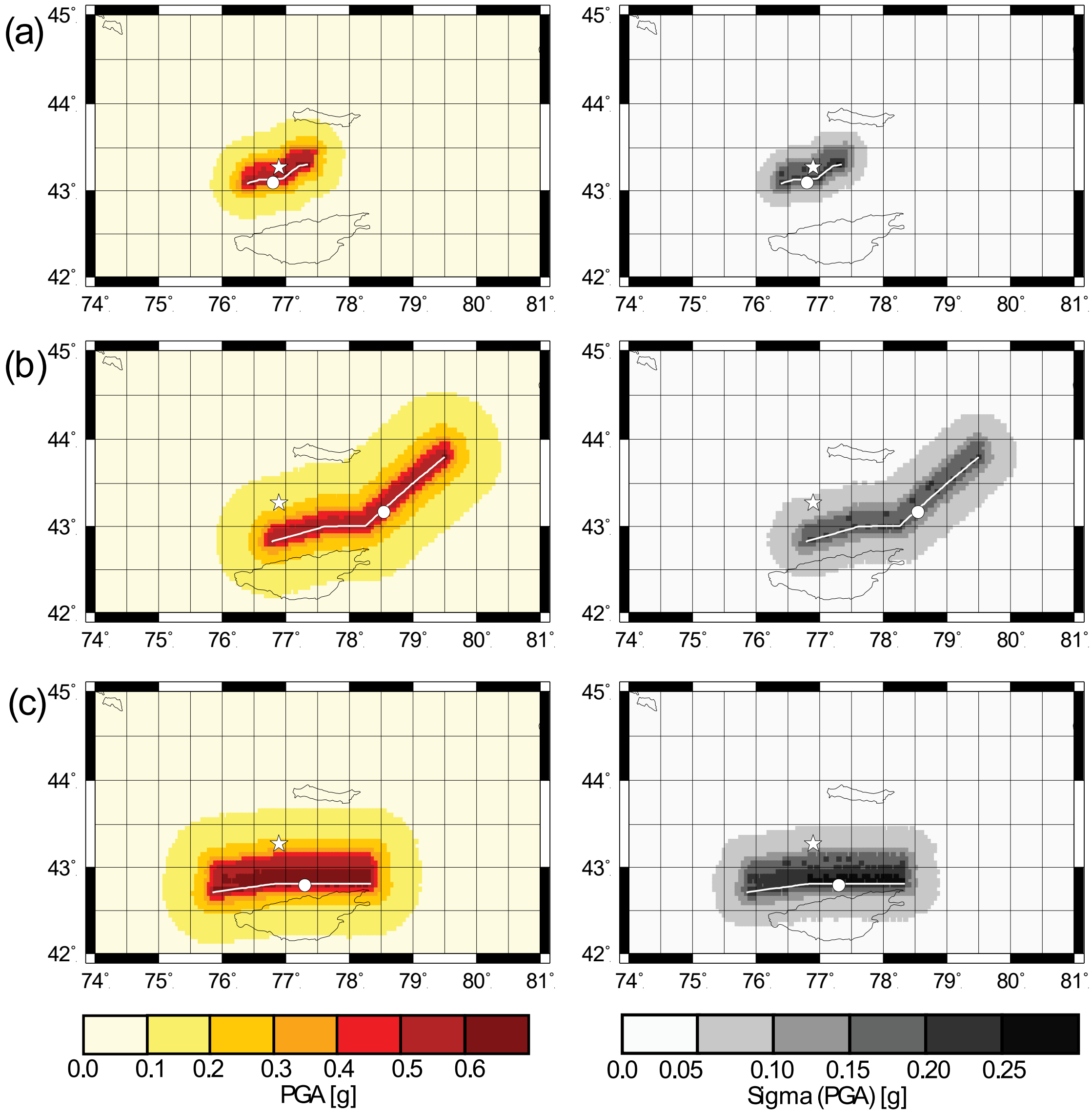

Figure 4: Distribution of PGA, together with its standard deviation, for (a) the 1887 Verny earthquake; (b) the 1889 Chilik earthquake; and (c) the 1911 Chon-Kemin earthquake. The mean ground motions and their standard deviations have been computed from 1000 scenarios. The white star indicates the city of Almaty. The white dot and the white line describe the epicenter and the fault rupture, respectively.

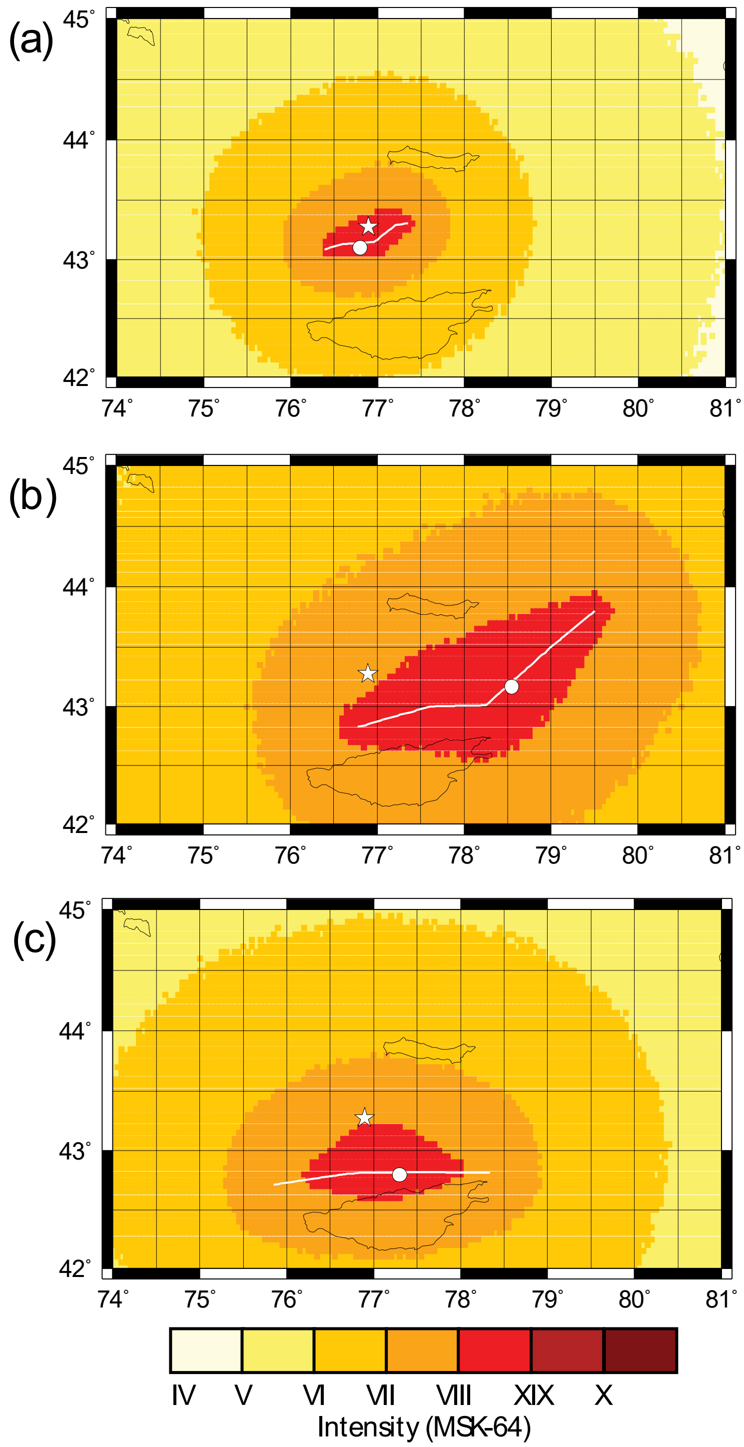

Figure 5: Distribution of MSK-64 intensity for (a) the 1887 Verny earthquake; (b) the 1889 Chilik earthquake; and (c) the 1911 Chon-Kemin earthquake. The white star indicates the city of Almaty. The white dot and the white line describe the epicenter and the fault rupture, respectively.

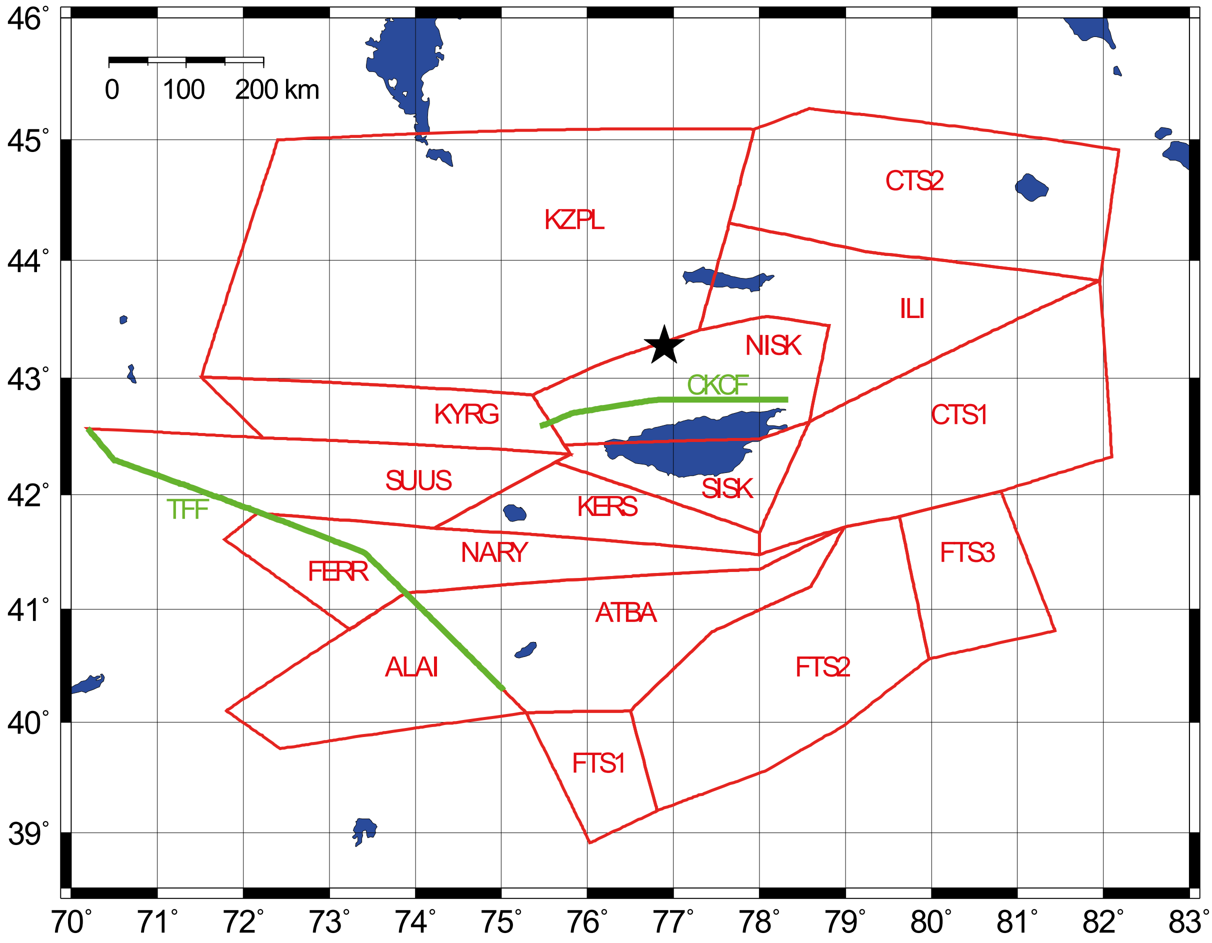

Figure 6: Seismic source model used in this study. The star denotes the site used for PSHA.

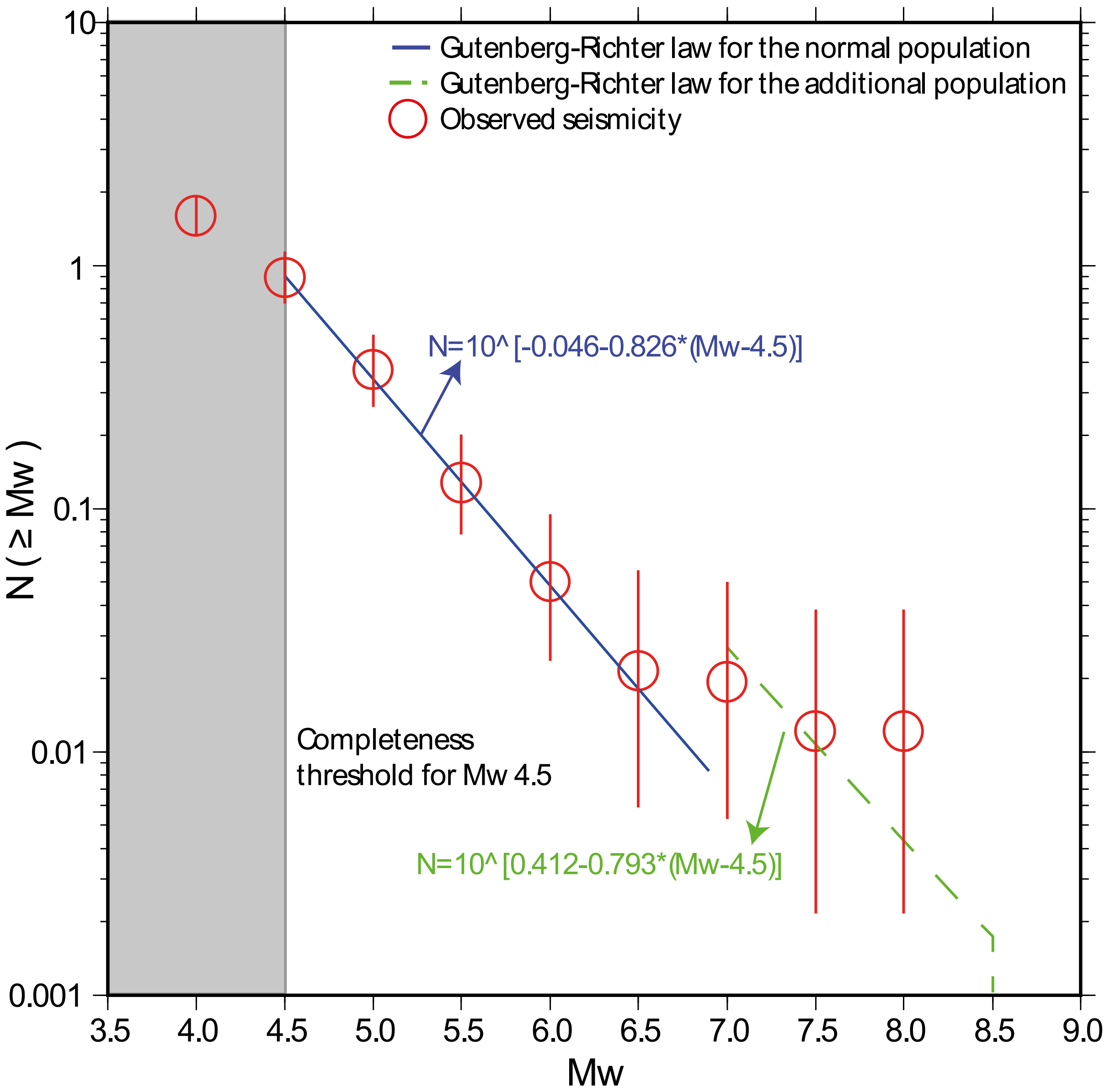

Figure 7: Magnitude-frequency recurrence for the source zone NISK. The solid line indicates the seismicity of the normal population of earthquakes predicted by the Gutenberg-Richter law in the range Mw 4.5 to 6.9; and the dashed line describes the seismicity of the additional population of earthquakes predicted by the Gutenberg-Richter law in the range Mw 7.0 to

8.5. The grey area describes the region outside the completeness threshold of the earthquake catalogue for Mw ≥ 4.5.

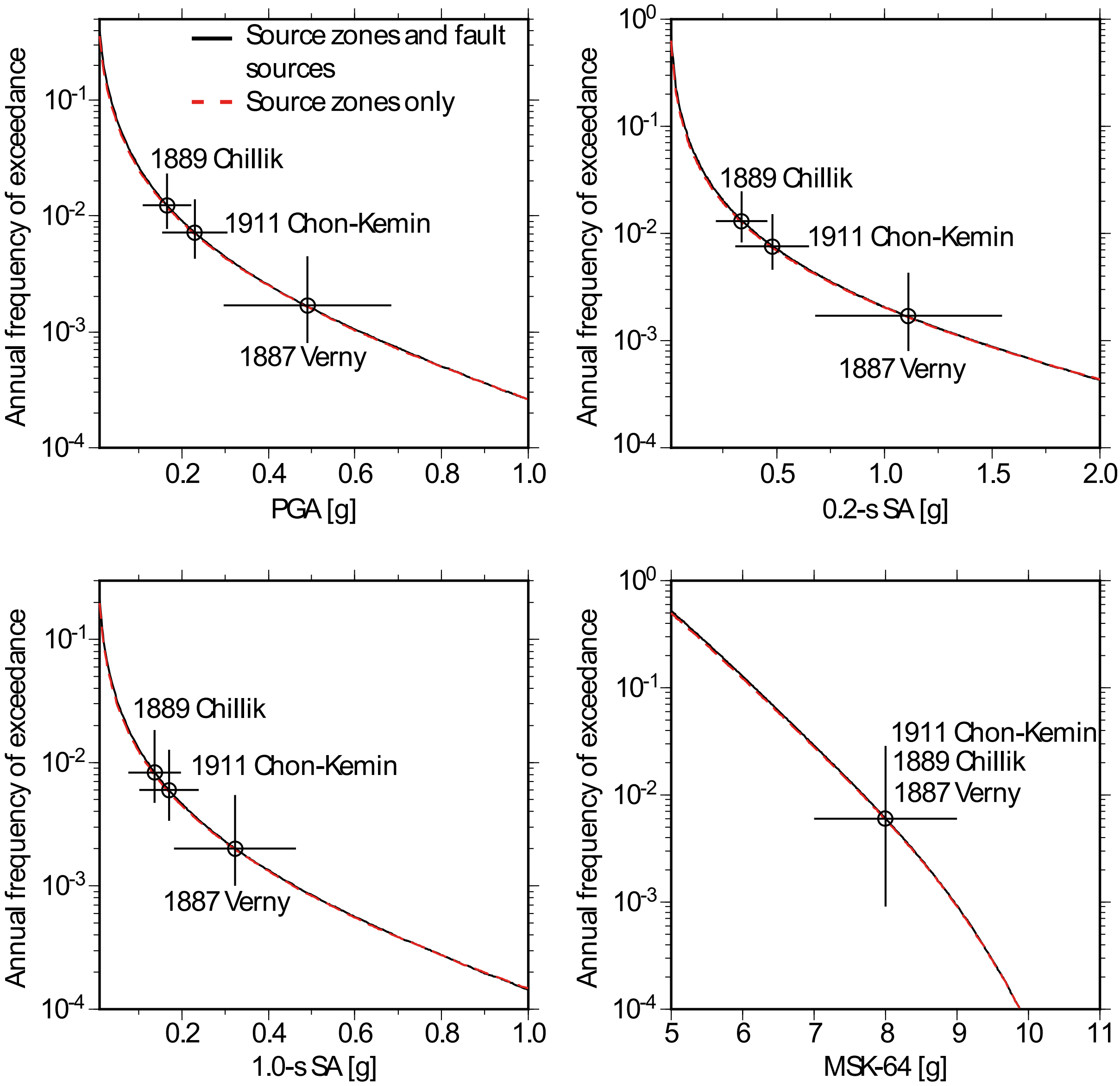

Figure 8: Seismic hazard curves for the site in Almaty. The solid lines are for the source model that consists of 16 zones and two faults; and the dashed lines are for the source model that consists of 16 zones only. The estimated ground motion values, together with their error-bars, for the scenario earthquakes are indicated by the circles.

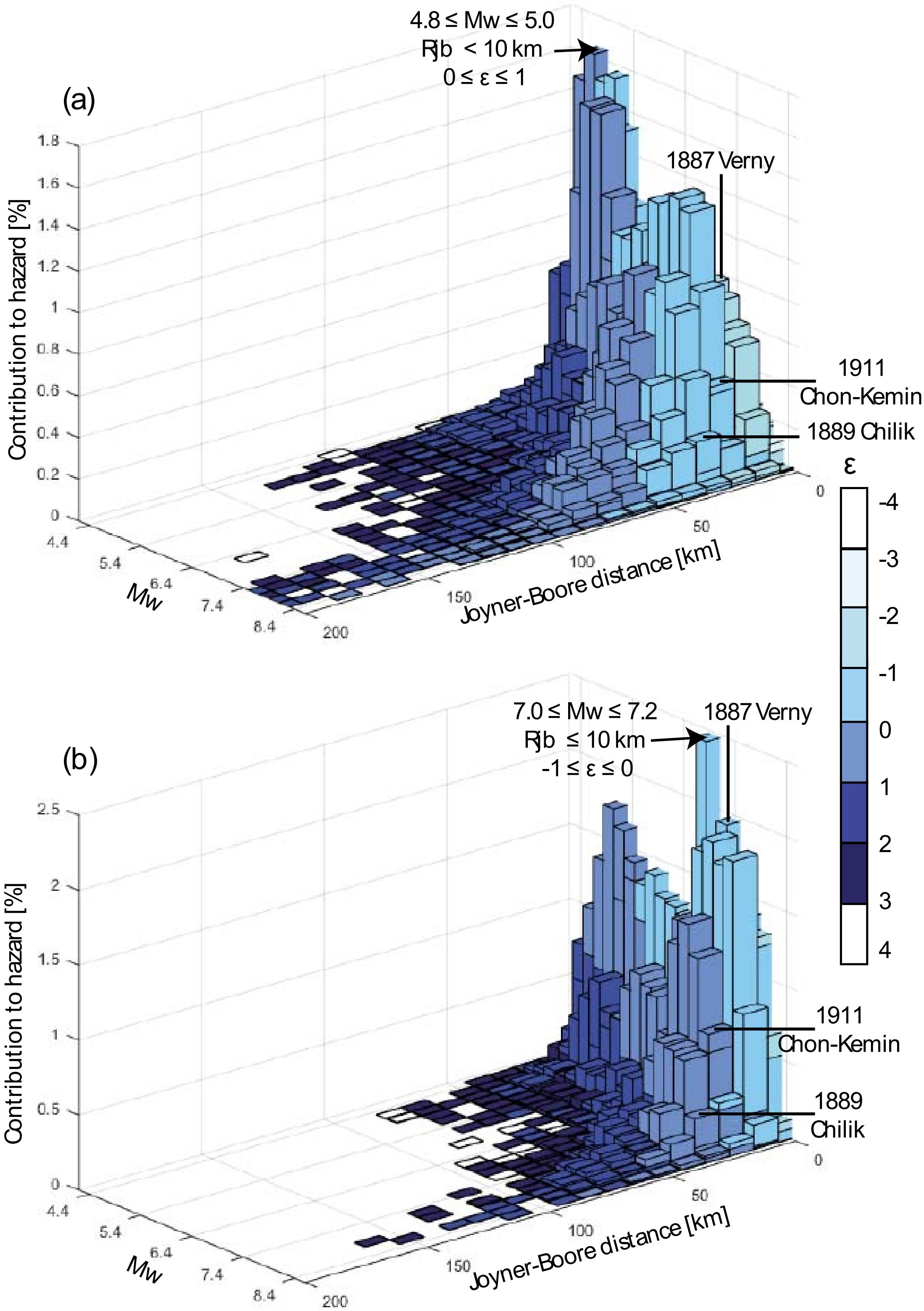

Figure 9: Disaggregation by magnitude Mw, Joyner-Boore distance and epsilon ε for two pairs of PGA values and return periods: (a) 0.23 ± 0.08 g and 139 ± 81 yr.; and (b) 0.49 ± 0.19 g and 588 ± 514 yr.

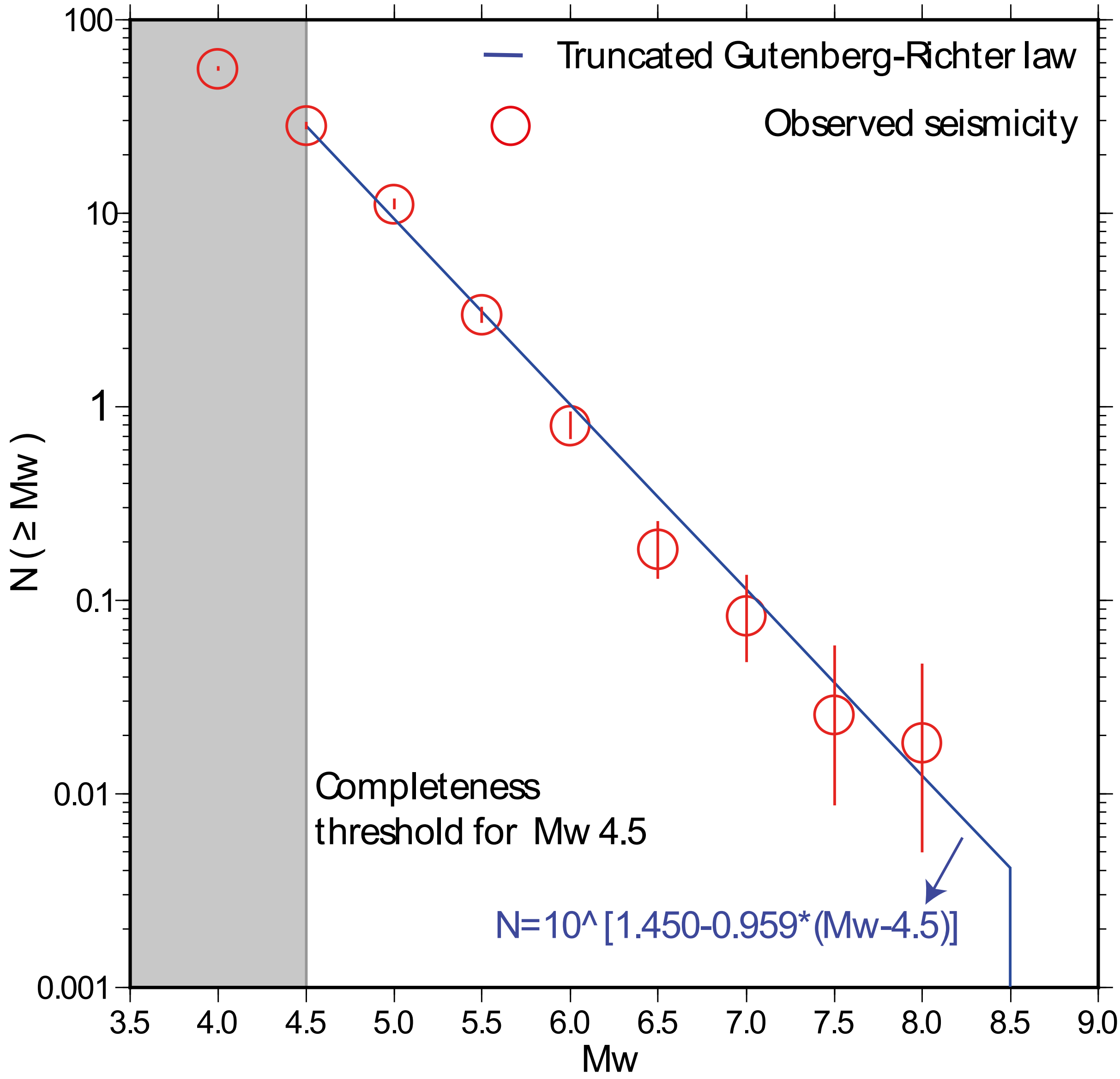

Figure B.1: Magnitude-frequency recurrence for the study area. The grey area describes the region outside the completeness threshold of the earthquake catalogue for Mw ≥ 4.5.

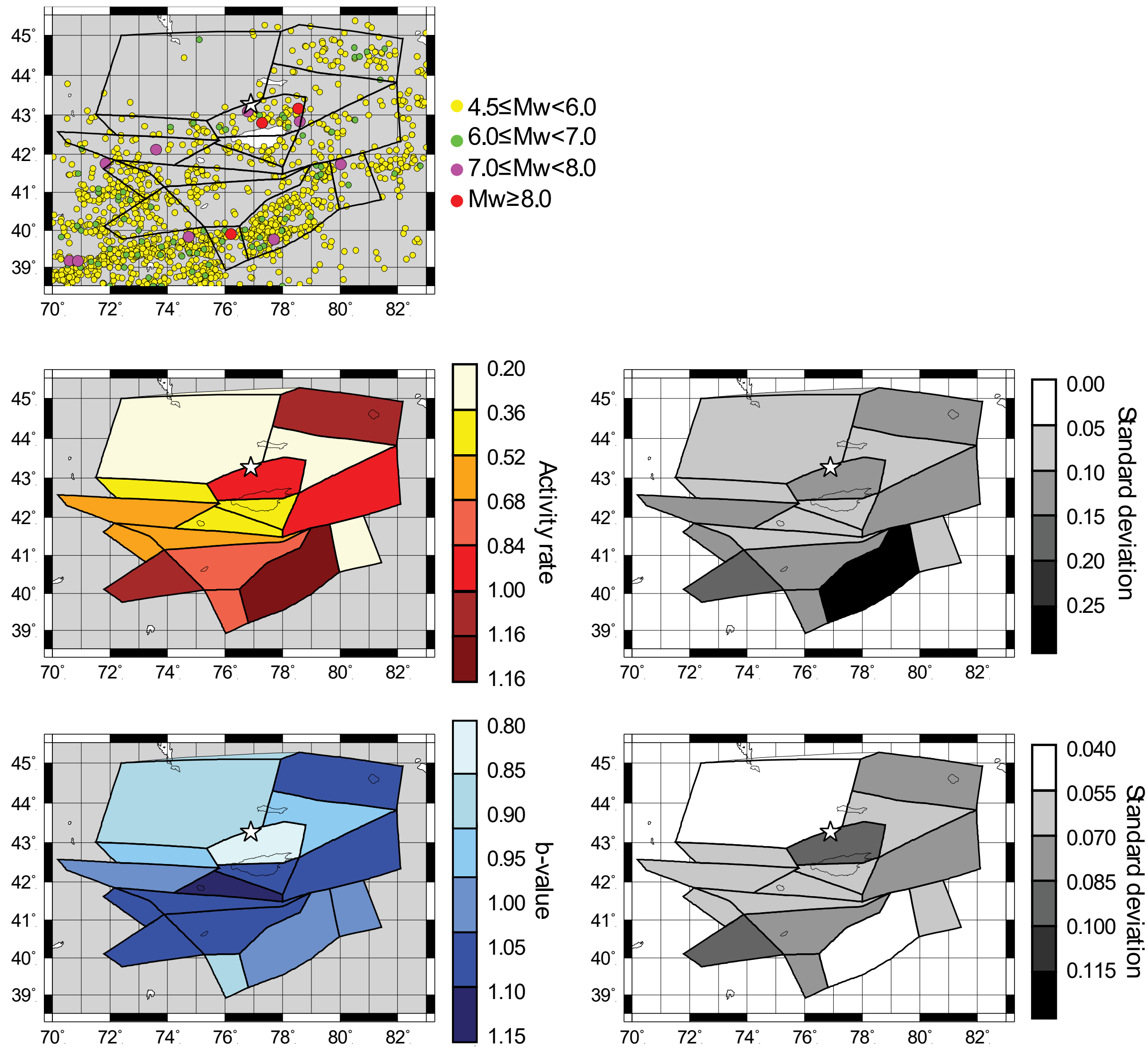

Figure B.2: Activity rates and b-values for the individual zones in the source model. (a) The earthquake catalogue within the completeness thresholds set out in Table A.2 and the source zone model. (b) The activity rate and (d) the *b*-value of each source zone, together with (c, e) the standard deviation (maps on the right). The white star denotes the site.

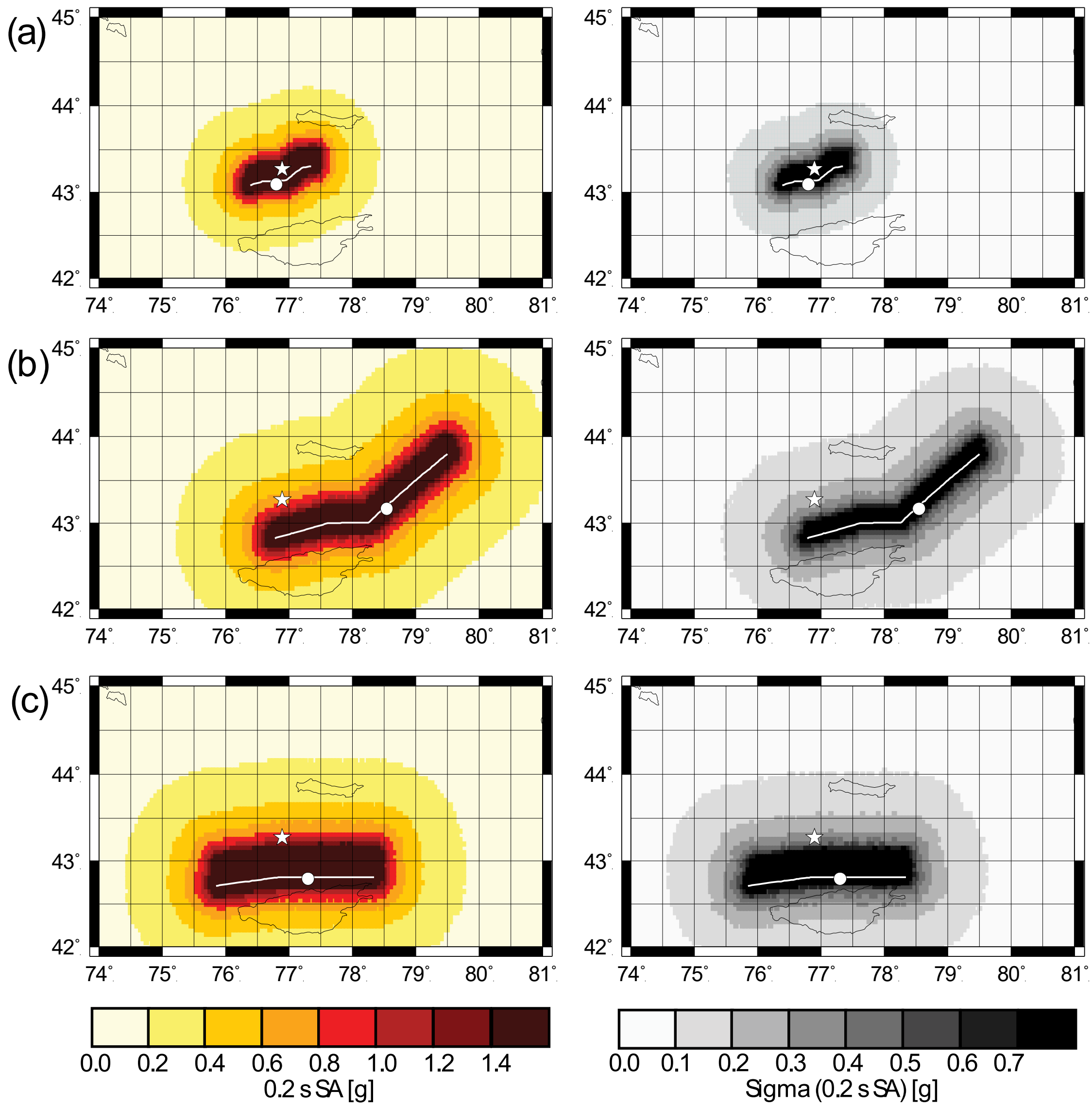

Figure C.1: Distribution of 0.2 s SA, together with its standard deviation, for (a) the 1887 Verny earthquake; (b) the 1889 Chilik earthquake; and (c) the 1911 Chon-Kemin earthquake. The mean ground motions and their standard deviations have been computed from 1000 scenarios. The white star indicates the city of Almaty. The white dot and the white line describe the epicenter and the fault rupture, respectively.

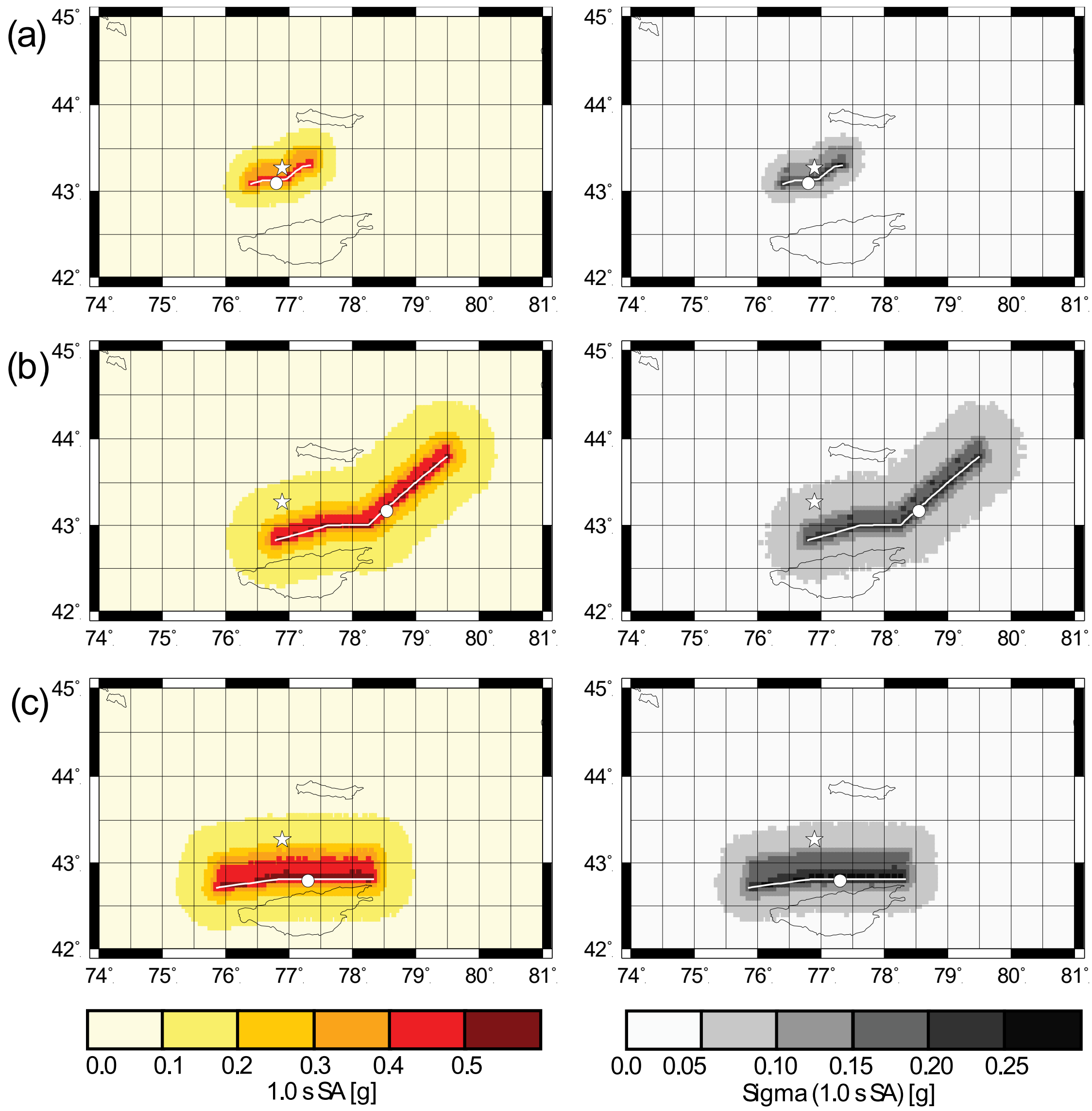

Figure C.2: Distribution of 1.0 s SA, together with its standard deviation, for (a) the 1887 Verny earthquake; (b) the 1889 Chilik earthquake; and (c) the 1911 Chon-Kemin earthquake. The mean ground motions and their standard deviations have been computed from 1000 scenarios. The white star indicates the city of Almaty. The white dot and the white line describe the epicenter and the fault rupture, respectively.

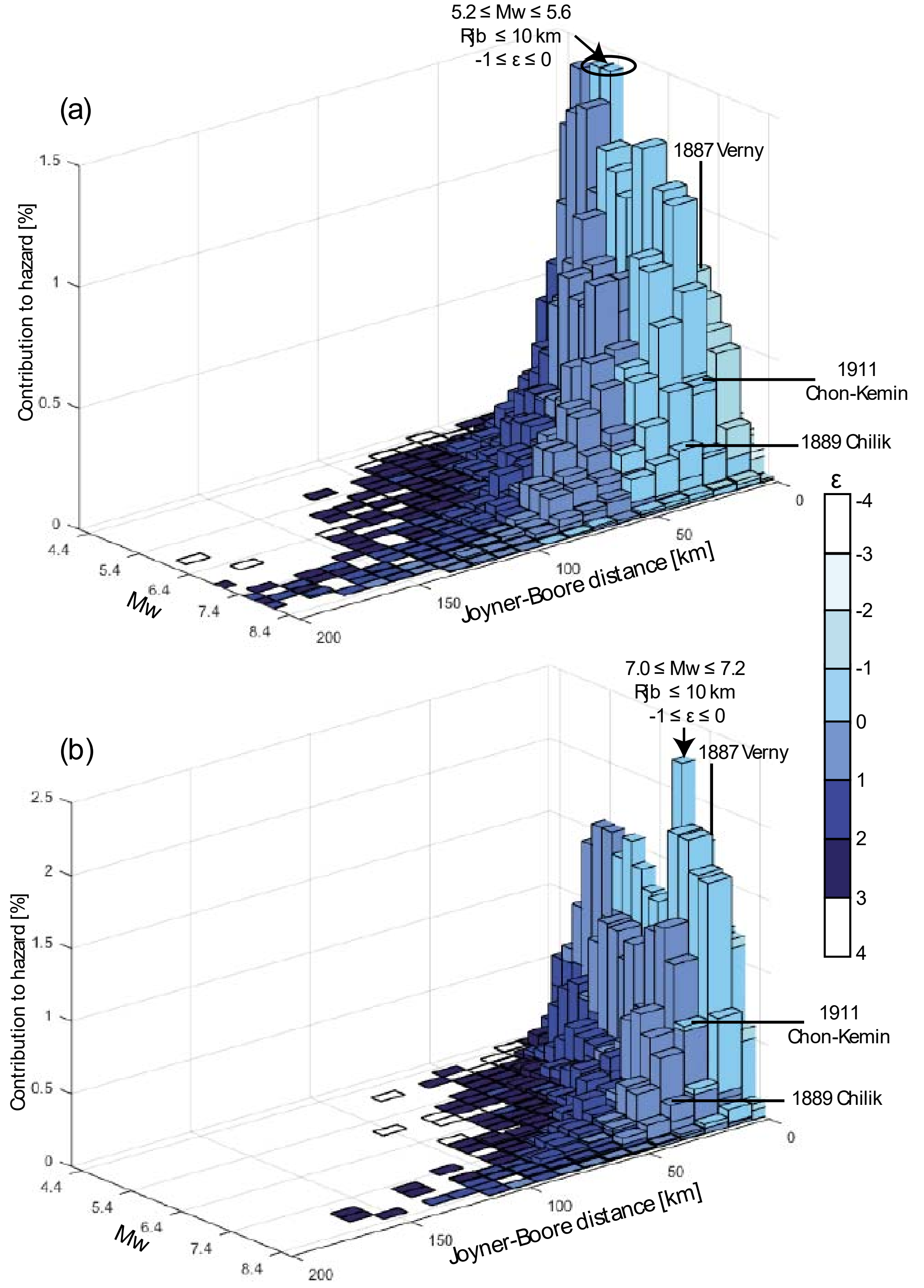

Figure C.3: Disaggregation by magnitude Mw, Joyner-Boore distance and epsilon ε for two pairs of 0.2 s SA values and return periods: (a) 0.48 ± 0.17 g and 132 ± 75 yr.; and (b) 1.11 ± 0.44 g and 588 ± 509 yr.

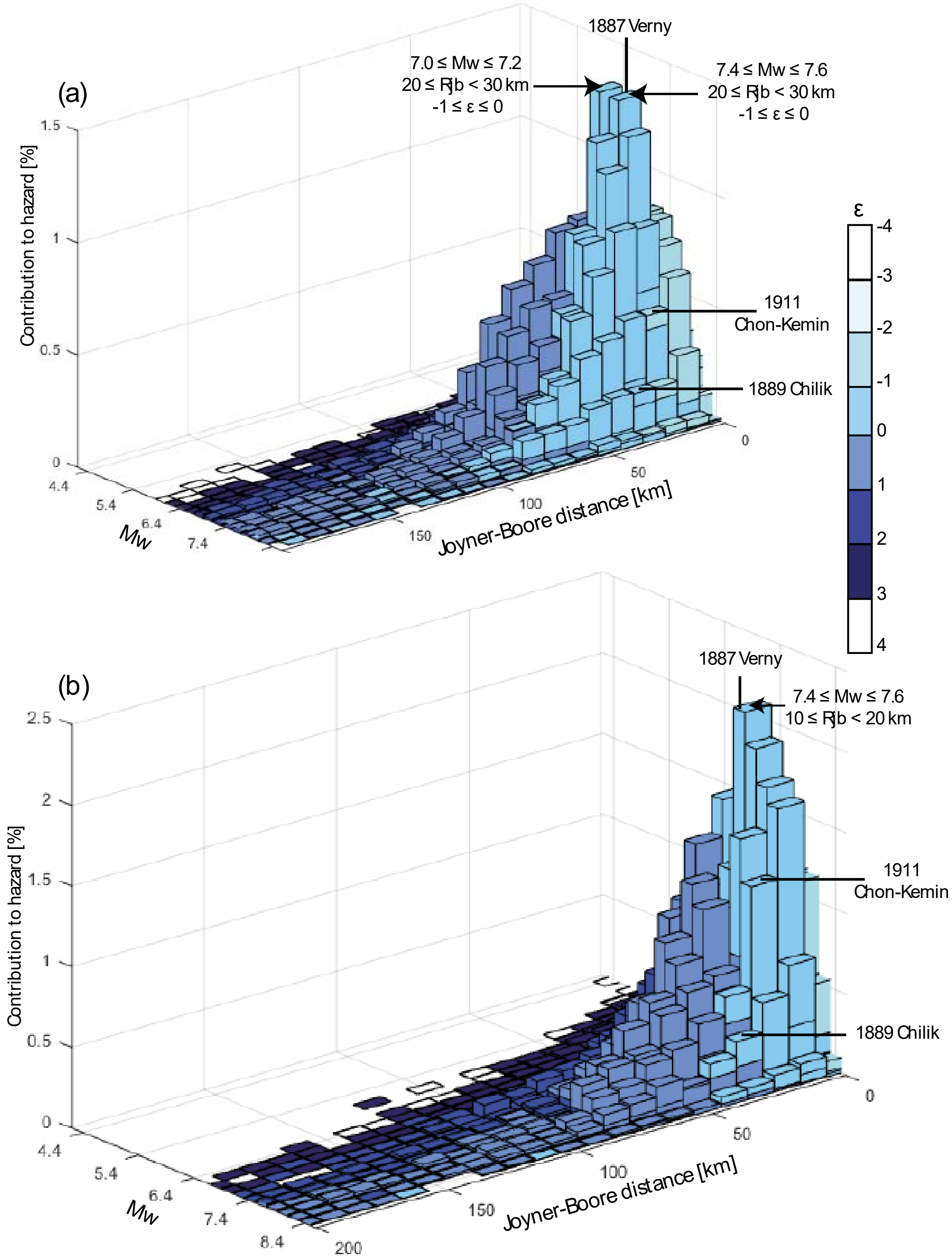

1466

1467 **Figure C.4:** Disaggregation by magnitude Mw, Joyner-Boore distance and epsilon ε for two
1468 pairs of 1.0 s SA values and return periods: (a) 0.17 ± 0.07 g and 167 ± 108 yr.; and (b) 0.32
1469 ± 0.14 g and 500 ± 409 yr.

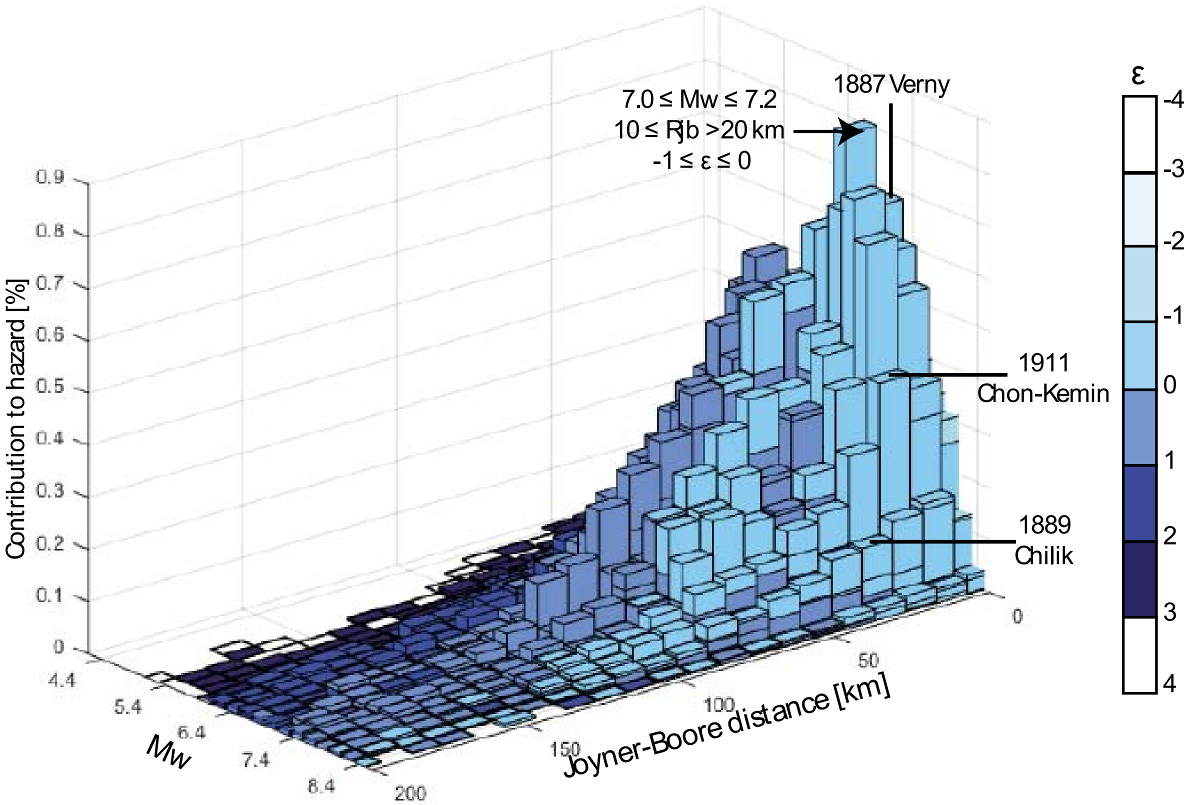

1470

1471 **Figure C.5:** Disaggregation by magnitude Mw, Joyner-Boore distance and epsilon ε for

1472 MSK-64 intensity VIII ± I and the return period of 161 ± 483 yr.

1473